การปลูกและวัดลักษณะสมบัติของแกลเลียมแอนติโมไนด์และอินเดียมแอนติโมไนด์ควอนตัมดอตบนแผ่นฐานลายตาราง

นายธนวร เพิ่มพูล

บทคัดย่อและแฟ้มข้อมูลฉบับเต็มของวิทยานิพนธ์ตั้งแต่ปีการศึกษา 2554 ที่ให้บริการในคลังปัญญาจุฬาฯ (CUIR)
เป็นแฟ้มข้อมูลของนิสิตเจ้าของวิทยานิพนธ์ ที่ส่งผ่านทางบัณฑิตวิทยาลัย
The abstract and full text of theses from the academic year 2011 in Chulalongkorn University Intellectual Repository (CUIR)
are the thesis authors' files submitted through the University Graduate School.

วิทยานิพนธ์นี้เป็นส่วนหนึ่งของการศึกษาตามหลักสูตรปริญญาวิศวกรรมศาสตรมหาบัณฑิต
สาขาวิชาวิศวกรรมไฟฟ้า ภาควิชาวิศวกรรมไฟฟ้า
คณะวิศวกรรมศาสตร์ จุฬาลงกรณ์มหาวิทยาลัย
ปีการศึกษา 2558

ลิขสิทธิ์ของจุฬาลงกรณ์มหาวิทยาลัย

GROWTH AND CHARACTERIZATION OF GaSb AND InSb QUANTUM DOTS ON CROSS-HATCH PATTERNS

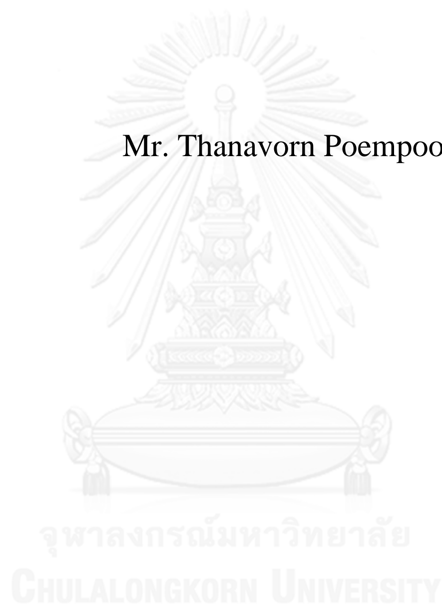

Mr. Thanavorn Poempool

A Thesis Submitted in Partial Fulfillment of the Requirements
for the Degree of Master of Engineering Program in Electrical Engineering
Department of Electrical Engineering
Faculty of Engineering
Chulalongkorn University
Academic Year 2015
Copyright of Chulalongkorn University

Thesis Title	GROWTH AND CHARACTERIZATION OF GaSb AND InSb QUANTUM DOTS ON CROSS-HATCH PATTERNS
By	Mr. Thanavorn Poempool
Field of Study	Electrical Engineering
Thesis Advisor	Associate Professor Songphol Kanjanachuchai, Ph.D.
Thesis Co-Advisor	Professor Somsak Panyakaew, D.Eng.

Accepted by the Faculty of Engineering, Chulalongkorn University in Partial Fulfillment of the Requirements for the Master's Degree

_______________________Dean of the Faculty of Engineering
(Professor Bundhit Eua-arporn, Ph.D.)

THESIS COMMITTEE

_______________________Chairman
(Professor Yasuhiko Arakawa, Ph.D.)

_______________________Thesis Advisor
(Associate Professor Songphol Kanjanachuchai, Ph.D.)

_______________________Thesis Co-Advisor
(Professor Somsak Panyakaew, D.Eng.)

_______________________Examiner
(Associate Professor Banyong Toprasertpong, Dr.Ing.)

_______________________External Examiner
(Noppadon Nuntawong, Ph.D.)

จุฬาลงกรณ์มหาวิทยาลัย
CHULALONGKORN UNIVERSITY

ธนวร เพิ่มพูล : การปลูกและวัดลักษณะสมบัติของแกลเลียมแอนติโมไนด์และอินเดียมแอนติโมไนด์ควอนตัมดอตบนแผ่นฐานลายตาราง (GROWTH AND CHARACTERIZATION OF GaSb AND InSb QUANTUM DOTS ON CROSS-HATCH PATTERNS) อ.ที่ปรึกษาวิทยานิพนธ์หลัก: รศ. ดร.ทรงพล กาญจนชูชัย, อ.ที่ปรึกษาวิทยานิพนธ์ร่วม: ศ. ดร.สมศักดิ์ ปัญญาแก้ว, หน้า.

วิทยานิพนธ์ฉบับนี้มุ่งเน้นไปที่การศึกษาผลการชี้นำของความเครียดจากลายตารางต่อการก่อตัวของควอนตัมดอตชนิดแกลเลียมแอนติโมไนด์ (GaSb) และอินเดียมแอนติโมไนด์ (InSb) ชั้นคั่นบาง GaAs หนา 6 นาโนเมตรที่ปลูกบน ชั้นลายตาราง $In_{0.17}Ga_{0.83}As$ หนา 30 นาโนเมตร บนแผ่นฐาน GaAs (001) ที่สังเคราะห์ด้วยเครื่องปลูกผลึกชนิดลำโมเลกุล (Molecular Beam Epitaxy, MBE) ถูกใช้เป็นแผ่นฐานแม่แบบลายตารางชี้นำ เทคนิคการปลูกสองวิธีที่ต่างกัน ได้แก่ เทคนิคพื้นฐาน (Conventional, MBE) และเทคนิคการปลูกแบบ MEE ถูกใช้สำหรับการปลูกควอนตัมดอตชนิดแอนติโมไนด์ สัณฐานวิทยาของควอนตัมดอตชนิด GaSb และ InSb ที่เรียงตัวเองบนลายตารางถูกศึกษาด้วยกล้องจุลทรรศน์ชนิดแรงอะตอม (Atomic force microscopy, AFM)

ควอนตัมดอตชนิด GaSb ที่ปลูกด้วยเทคนิค MEE แสดงผลการเรียงตัวบนแนวสันของลายตารางอย่างชัดเจน เมื่อเทียบกับควอนตัมดอตที่ปลูกด้วยเทคนิคพื้นฐานซึ่งควอนตัมดอตกระจายไปทั่วบริเวณ ความสูงเฉลี่ยของควอนตัมดอตชนิด GaSb ที่ก่อตัวบนแนวสันของลายตารางที่ปลูกด้วยเทคนิค MEE สูงเกือบสองเท่าของควอนตัมดอตชนิด GaSb ที่ปลูกด้วยเทคนิคพื้นฐาน นอกจากนี้แบบจำลองอย่างง่ายถูกเสนอเพื่อแสดงกลไกการก่อตัวของควอนตัมดอตชนิด GaSb บนแนวสันของลายตาราง ในทางกลับกัน ความเครียดชนิดบีบอัดจากแนวสันของลายตารางไม่มีผลต่อการก่อตัวของควอนตัมดอตชนิด InSb บนแนวสันของลายตาราง อีกทั้ง ควอนตัมดอตชนิด InSb ยังชอบก่อตัวตรงบริเวณพื้นผิวเรียบอันปรากฏการมีอยู่ของความเครียดชนิดยืดขยาย ผลการวัดเชิงแสงที่เปล่งจากผิวข้างของชิ้นงานควอนตัมดอตชนิด GaSb ที่ปลูกด้วยเทคนิค MEE แสดงค่ายอดพลังงานที่ประมาณ 0.73-0.75 และ 1.14 อิเล็กตรอนโวลต์ ซึ่งสองค่ายอดพลังงานนี้สอดคล้องกับการเปลี่ยนผ่านพาหะระหว่างโครงสร้างควอนตัมดอตชนิด GaSb กับ InGaAs และกับ GaAs ตามลำดับ

จุฬาลงกรณ์มหาวิทยาลัย
Chulalongkorn University

ภาควิชา	วิศวกรรมไฟฟ้า	ลายมือชื่อนิสิต	....
สาขาวิชา	วิศวกรรมไฟฟ้า	ลายมือชื่อ อ.ที่ปรึกษาหลัก	....
ปีการศึกษา	2558	ลายมือชื่อ อ.ที่ปรึกษาร่วม	....

5770421021 : MAJOR ELECTRICAL ENGINEERING
KEYWORDS: CROSS-HATCH PATTERNS, GASB QUANTUM DOTS, INSB QUANTUM DOTS

THANAVORN POEMPOOL: GROWTH AND CHARACTERIZATION OF GaSb AND InSb QUANTUM DOTS ON CROSS-HATCH PATTERNS. ADVISOR: ASSOC. PROF. SONGPHOL KANJANACHUCHAI, Ph.D., CO-ADVISOR: PROF. SOMSAK PANYAKAEW, D.Eng., pp.

This thesis is dedicated to study guiding effect of strain from cross-hatch pattern (CHP) to GaSb quantum dot (QD) and InSb QD nucleation. A 6-nm GaAs spacer on 30-nm $In_{0.17}Ga_{0.83}As$ CHP on GaAs (001) substrate, fabricated by molecular beam epitaxy (MBE), is used as the CHP guiding template. Two different growth techniques-Conventional and Migration Enhance Epitaxy (MEE)-are performed for the antimonide QDs growth. The morphology of self-aligned GaSb and InSb QDs on CHP are characterized by atomic force microscopy (AFM).

The GaSb QDs grown by MEE shows the obvious nucleation on the CHP ridges compares to the QDs grown by MBE, which QDs distribute all over the areas. The average height of GaSb QDs, formed on the CHP ridges, grown by MEE is almost doubled that of GaSb QDs grown by MBE. Moreover, a simple descriptive model is proposed to demonstrate the GaSb QD formation mechanism on CHP ridges. In contrast, the compressive strain from CHP does not affect the nucleation of InSb QDs on the ridges because the InSb QDs prefer to nucleate on the flat areas where the tensile strain exists. The photoluminescence (PL) spectra from side-emission of GaSb QDs grown by MEE shows the energy peaks at ~0.73-0.75 eV and ~1.14 eV. These two peaks correspond to carrier transitions between GaSb QDs and InGaAs and GaAs, respectively.

Department:	Electrical Engineering	Student's Signature	....
Field of Study:	Electrical Engineering	Advisor's Signature	....
Academic Year:	2015	Co-Advisor's Signature	....

ACKNOWLEDGEMENTS

Foremost, I would like to express my sincere gratitude to my advisor, Assoc. Prof. Dr. Songphol Kanjanachuchai, for his valuable help, patience, motivation, enthusiasm, and immense knowledge, and his guidance throughout the research period. I would not have achieved this far and this thesis would not have been completed without all the support that I have always received from my advisor.

Besides my advisor, I would like to give thanks to my co-advisor, Prof. Dr. Somsak Panyakeow, for his encouragement and many research opportunities that I had received.

Moreover, I would like to thank the rest of my thesis committee: Prof. Dr. Yasuhiko Arakawa, Assoc. Prof. Dr. Banyong Toprasertpong, and Dr. Noppadol Nuntawong, for their insightful comments, and hard questions that opened up the ideas for the researches and improvements.

I would like thanks to the SDRL staffs, Mr. Supachok Thainoi, Mr. Pattana Phuntumwong, and Mrs. Kwanruan Thainoi, for their technical support.

In addition, I would like to thank to my fellow lab members in SDRL: Mr. Apichart Jittrong, Mr. Win Eiwwongcharoen, and Mr. Nitas Nakareseisoon for the funny moments we had together. Also, I would like to thanks Mr. Samatcha Vorathamrong, and Patchareewan Prongjit for their firs time mentoring me on operating new MBE system. In particular, I am grateful to Miss Zon for her calibration during my research.

Last but not least, I would like to give a special thanks to my family: my parents for their love and support throughout my life. Whenever I felt down, they always be there for me. Also thanks to my sister and brother who always stay side-by-side in my entire life.

This research was funded by the Research Chair Grant, the National Science and Technology Development Agency (NSTDA), Thailand, Thailand Research Fund (TRF, RSA5880049), Nanotechnology Center of Thailand (NANOTECH), Asian Office of Aerospace Research and Development (AOARD) (Grant No. FA2386-14-1-4081), and Ratchadapisek Sompoch Endowment Fund (2015), Chulalongkorn University (CU-58-051-EN).

CONTENTS

Page

THAI ABSTRACT ... iv
ENGLISH ABSTRACT ... v
ACKNOWLEDGEMENTS ... vi
CONTENTS ... vii
LIST OF FIGURES ... ix
LIST OF TABLES ... xii
CHAPTER 1 INTRODUCTION ... 1
CHAPTER 2 THEORETICAL BACKGROUND ... 4
2.1 Heteroepitaxy ... 4
2.2 Lattice Mismatch ... 5
2.3 Stress and Strain Relaxation ... 6
2.4 Dislocations and Surface Steps ... 7
2.5 Cross-Hatch Patterns ... 9
2.5.1 Cross-Hatch Formation Mechanism ... 10
2.6 Island Formation Mechanisms ... 11
2.7 Low-Dimensional Nanostructure: Quantum Dots ... 13
CHAPTER 3 FABRICATIONS AND CHARACTERIZATION TECHNIQUES ... 16
3.1 Molecular Beam Epitaxy ... 16
3.2 Reflection High Energy Electron Diffraction ... 18
3.3 Pre-Fabrication Processes ... 20
3.3.1 Sample Preparation ... 20
3.3.2 Temperature Calibration ... 21
3.3.3 Growth-Rate Calibration ... 22
3.3.3.1 Growth-Rate Calibration for GaAs ... 23
3.3.3.2 Growth-Rate Calibration for InAs ... 24
3.3.4 GaAs Buffer Deposition ... 25
3.4 Fabrication Processes ... 25
3.4.1 CHP and GaAs Spacer ... 25

Chulalongkorn University

Page

3.4.2 Quantum Dots Growth 26
3.4.2.1 Conventional Method 26
3.4.2.2 Migration Enhance Epitaxy 27
3.4.3 GaAs Capping Layer 28
3.5 Post-Growth Characterizations 28
3.5.1 Atomic Force Microscopy 28
3.5.2 Photoluminescence 29
CHAPTER 4 GaSb AND InSb ON CROSS-HATCH PATTERNS 31
4.1 CHP Growth Details 31
4.2 Optimizing CHP Template 32
4.3 GaSb on CHP Grown by Conventional and MEE Methods 36
4.3.1 Morphology 36
4.3.2 Size Distribution 41
4.3.3 Optical Property of GaSb QDs on CHP 44
4.4 InSb on CHP 47
4.4.1 Morphology: Effect of Growth Temperatures 48
4.4.2 Morphology: Effect of MEE Technique 49
CHAPTER 5 CONCLUSIONS 52
..... 54
REFERENCES 54
VITA 60

จุฬาลงกรณ์มหาวิทยาลัย
CHULALONGKORN UNIVERSITY

LIST OF FIGURES

Figure 2.1 Energy gap and lattice constant of III-V compound semiconductors at room temperature. 6

Figure 2.2 Diagram of (a) compressive strain and (b) tensile strain in InGaAs/GaAs system. 7

Figure 2.3 (a) Misfit and Threading dislocation that occur in heteroepitaxial deposition and (b) dislocation vector that occur from edge dislocation and screw dislocation [22]. 8

Figure 2.4 Surface step elimination process during CHP growth. (a) The accumulation of compressive strain in the 2D film. (b) Dislocation and surface steps at critical thickness. (c) Surface step elimination of overgrown layer [24]. 8

Figure 2.5 AFM image of cross-hatch pattern in InGaAs and GaAs [9]. 9

Figure 2.6 Critical thickness of 60˚- dislocation (h_{c60}) and In content of $In_xGa_{1-x}As$ [37]. 11

Figure 2.7 Equilibrium phase diagram of different growth modes as a function of H (layer thickness) and ε (strain). The first and last row images illustrate the nano-structures on the surface in different six growth modes. The small triangles represent the quasi-stable island and the large-shaded triangles represent the ripening islands. At the middle image, each limitation for each growth modes is drawn in their own boundaries as follows. $H_{c1}(\varepsilon)$: FM-R_1, FM-SK_1; $H_{C2}(\varepsilon)$: SK_1-R_2; $H_{C3}(\varepsilon)$: SK_2-SK_1; $H_{C4}(\varepsilon)$ VW-SK_2, VW-R_3 [38]. 12

Figure 2.8 Schematic views and density of states (DOS) of (a) bulk, (b) quantum wells, (c) quantum wires and (d) Quantum dots [40]. 14

Figure 3.1 Cross-sectional diagram of the growth chamber in MBE system. The main components are effusion cells, RHEED system and gauge flux measurement. 17

Figure 3.2 Molecular Beam Epitaxy, RIBER Compact-21T with an external Sb cracker installation. 18

Figure 3.3 Schematic diagram of RHEED geometry. The elongated spots indicate the intersection of the Ewald sphere with the (01), (00), and (0-1) rods. 19

Figure 3.4 (a) Streaky pattern, and (b) spotty pattern. 19

Figure 3.5 Temperature profile for pre-heating process. 20

Figure 3.6 Schematic diagram of [1-10] azimuth RHEED pattern transition during temperature calibration process. 22

Figure 3.7 (a) two-dimensional GaAs layer formation on GaAs (001) [46].............23

Figure 3.8 RHEED intensity oscillation of GaAs taken in this experiment. Square box in inset image indicates the specular beam spot that used for intensity observation. 24

Figure 3.9 Schematic of strained GaAs/InGaAs/GaAs system.................................26

Figure 3.10 Shutter sequence of Sb and group-III atoms in antimonide QDs growth by (a) conventional method, and (b) migration enhance epitaxy. 27

Figure 3.11 (a) Atomic force microscopy (AFM), and (b) systematic diagram of AFM. 28

Figure 3.12 Experimental set-up diagram of photoluminescence measurement. 30

Figure 4.1 Schematic diagram of the CHP structure. ***d*** is the InGaAs thickness........32

Figure 4.2 The schematic diagram of strain energy distribution in a function of position of one-dimensional island. The filled and empty squares are represented the atoms of substrate and the island [51]. 33

Figure 4.3 The schematic diagram of strain field, $\varepsilon(x)$, of two one-dimensional islands with different island width, s_1 and s_2 which s_2 is smaller than s_1. The two islands are separated by a distance L much greater than s_1 and s_2 [52]. 34

Figure 4.4 10×10 μm^2 AFM images of CHP with thickness of (a) 40 nm, and (b) 30 nm, respectively. 35

Figure 4.5 Cross-sectional CHP template for antomonide QDs growth. The optimal CHP thickness is 30 nm. 35

Figure 4.6 (a) and (b) are the 5×5 μm^2 AFM images of GaSb QDs, grown by MBE technique, shown in NC force and height field image mode, respectively. (c) and (d) are 5×5 μm^2 AFM images, grown by MEE technique, shown in NC force and height field image mode, respectively. 38

Figure 4.7 Illustration diagrams of the mechanism of GaSb QDs formation, grown by MEE technique, on a CHP ridge. (a) and (b) are the images show the before and after nucleation. 40

Figure 4.8 Histogram of height distribution of GaSb QDs grown by conventional method, (a) and (b), and MEE method (c). The size distribution was measured on (a) flat area, and (c), (d) along CHP ridges. The Gaussian curve fit and the center position of the Gaussian peak are shown in the figures....42

Figure 4.9 (a) and (b) are the selected area of AFM images of GaSb QDs, grown by MBE and MEE, respectively. The elongated GaSb QDs are highlighted in the dashed circles. (c) is the shape configurations of some QDs found on the CHP ridge and (d) is the shape configuration of most QDs found on flat area with their particular line profiles. 44

Figure 4.10 5×5 μm^2 AFM image of the re-grown GaSb QDs on CHP. The arrows indicate some oval defects. 45

Figure 4.11(a) Power-dependent PL spectrum of GaSb QDs grown by MEE technique. The QD peaks are found at ~0.73-0.75 eV and ~1.14 eV as denote by the arrows. (b) is a schematic diagram of carriers transitions in GaSb QDs structure. 46

Figure 4.12 5×5 μm^2-AFM images of InSb QDs, grown at (a) 400˚C and (b) 300˚C and their particular height contrast image mode. 48

Figure 4.13 Elongated shape of InSb QDs along [110]. 49

Figure 4.14 (a) 5×5 μm^2 and (b) 10×10 μm^2 modified color AFM image of InSb QDs on CHP template, grown by MEE technique at substrate temperature of 300°C. 50

Figure 4.15 The shape configurations of InSb QDs found on the CHP template and the line profiles. 51

LIST OF TABLES

Table 2.1 Fundamental properties of GaAs, $In_xGa_{1-x}As$, GaSb, and InSb 5
Table 4.1 Growth condition for GaSb QDs on CHP..36
Table 4.2 Average height of GaSb QDs...41

CHAPTER 1
INTRODUCTION

The rapid development in semiconductor technology in the twentieth century affects the improvement of electronic devices and communication technology. Tracing back to the origin of the first electronic devices, silicon is the first semiconductor element that played the role and had revolutionized in microelectronic industry. But the electronic property of silicon is an indirect-band gap which exhibits only electrical property. As the time went by, the growing of optical communication technology has also risen up parallel to electronics technology. That means such this technology requires the optically- exhibited devices, optoelectronics devices. One of the devices is the semiconductor device that can respond to long wavelength covers from mid- to far-infrared. Applications could include IR detector, gas detector, high-speed data processing, communications [1], and narrow band gap solar cells.

Antimony (Sb)-based binary compounds such as aluminium antimonide (AlSb), gallium antimonide (GaSb), and indium antimonide (InSb) are used as the main electronic material for such devices. Due to the existence of narrow energy band gap, Sb-based devices can be candidates for high-frequency [2] and low-power electronic devices [1]. So, III-V compound with a direct-band gap semiconductor has been researched prior to improve and develop particular devices. The strong emission and absorption in their characteristics give rise in devices' performance such as detection and emission. The performance of the devices mostly depends on the composition of III-V alloying materials (i.e. GaAs, InAs, InP, InGaAs, GaSb, InSb) which the energy band alignment can be engineered. This band gap engineering empowers the formation of heterojunction by epitaxial deposition.

Epitaxy is a deposition method which the single crystals are deposited on another crystal arrangement. Epitaxial layer can be classified into two types, according to their used crystals between substrate and deposition layer: *homoepitaxy*, and *heteroepitaxy*. If the substrate and the deposited layer are the same materials, it is

said to be homoepitaxial deposition. Contrary, the heteroepitaxy is the system where the used materials between deposition layer and substrate are differences. Both homoepitaxy and heteroepitaxy can be synthesized by either physical based- or chemical based-method. The example of epitaxy methods are liquid phase epitaxy (LPE), chemical vapor deposition (CVD), metal organic chemical vapor deposition (MOCVD), and molecular beam epitaxy (MBE). The latter approach, MBE, is an deposition technique operates under ultra-high vacuum condition which the deposited layer can be controlled down to monolayer scale and leads to the nanostructure formation.

Quantum dot (QD) is one of the nanostructures that have been on focus since it was predicted and expected to further development in some applications. Due to the physical aspects in size that have reach to the quantum limit where the quantum confinement, discretized in energy level, and tunneling effect etc. exist, this quantum structures become interesting in quantum physics and device engineering. Scaling-down the structure is promising possibility for improving novel devices in both electronic and optoelectronic devices.

QD is formed by lattice-mismatched heteroepitaxy. When one material is deposited on another material with difference lattice constant to the first one, the compressive strain is induced until the film thickness increases beyond the critical thickness, lastly, resulting in strain relaxation. At this stage the formation of such nanostructure is occurred. In general, the self-assembled QDs form randomly throughout the material surface [3, 4]. However, there are some novel applications which require the ordering of QDs which they manifest some phenomena such as quantum coupling, spin property etc.[5, 6]. These properties can be used in, for instance, lasers, logic computing devices, and single electron transistors. Many attempts have been tried to engineer and develop the quantum nanostructure where its nucleation site can be controlled.

There are two methods that have been used in controlling the ordering of the quantum nanostructures. The first one is force alignment template. This method, the substrate is patterned by electron beam, lithography [7] or by using high index

substrate. The drawback of this method is the unpleasant defects during the process which distorts both electronics and optical properties of the devices. Another method is self-aligned QDs from the strained pattern. The proper strain energy on the material surface is the key factor in strain engineering for guiding QDs to nucleate on particular position. This method can be created by the strain from super-lattice template [8], and cross-hatch pattern (CHP) [9, 10].

Cross-hatch pattern is a self-relieved pattern in heteroepitaxial deposition. The material systems such as InGaAs/GaAs [9, 11], InGaAs/InP, GaAsP/GaAs [11], GaAs/Si [11], and SiGe/Si [11]. CHP is generated from two types of dislocation: (1) misfit dislocation (MD) is a type of dislocation at the interface between two materials. (2) Threading dislocation (TD) is a mobile MD that has threaded up from the interface to the top epitaxial layer and causes a diffused strain throughout the surface. Strain will be relaxed when deposition layer are thicker beyond the critical thickness and results in the ridge patterns undulate orthogonally in [1-10]- and [110]- crystallographic direction. This CHP can be used as a template to guide QDs nucleation.

This thesis is aimed to fabricate GaSb QDs and InSb QDs on $In_xGa_{1-x}As$ CHP by using MBE. The conventional growth and migration enhance epitaxy (MEE) will be performed on the QDs growth to study the kinetic aspects on guiding effect of $In_xGa_{1-x}As$ CHP to antimonide QDs. Finally, the morphology and optical property will be carried out by atomic force microscopy (AFM) and photoluminescence (PL), respectively to get understanding in fundamental properties.

CHAPTER 2
THEORETICAL BACKGROUND

The details found in this chapter are mainly about epitaxy. Each section explains in about the origin of quantum dots formation and the cross-hatch patterns formation which are the core structures/patterns for studying strain-guided quantum dots formation in this thesis. The common principles bases on lattice-mismatched, strain relaxation, defects and surface step as introduce in section 2.2, 2.3 and 2.4, respectively. In section 2.5 and 2.6, the mechanism on cross-hatch patterns formation and low-dimensional structures will be given in details.

2.1 Heteroepitaxy

Epitaxy is a deposition of single crystal layer on top of a crystalline substrate, which the successive deposited film is called epitaxial layer. The epitaxial layer can be fabricated by, for example, Vapor Phase Epitaxy (VPE) [12], Liquid Phase Epitaxy (LPE) [13], and Molecular Beam Epitaxy (MBE) [14].

The epitaxial growth is very useful for the applications that require highly quality for a deposited layer, such as heterojunction bipolar transistors, LEDs, and lasers [15]. Moreover, epitaxy can be classified into two types; they are homoepitaxy and heteroepitaxy. Homoepitaxy is the growth of a layer of the same material as the substrate, where the atomic arrangement in two layers is matching together.

The growth of homoepitaxy is commonly used to apply for growing high purity film and used to control the doping profiles [16]. In contrary, heteroepitaxy is different. Heteroepitaxy is the growth of layer of different materials other than the substrate, as the growth of GaAs/Si can be an example. The presence of different in materials result in different lattice-mismatched which can manifest other low-dimensional structures other than two-dimensional thin films. Yet, some electronic and optical properties of the structures changes. The effect of lattice-mismatched is given in section 2.2.

2.2 Lattice Mismatch

Lattice constant, *a*, is one of the specific parameter to each elements and compounds. There are two types of lattice forming during material deposition; (1) lattice-matched, and (2) lattice-mismatched systems. In the case of lattice-matched, the deposited layer has the same or almost the same lattice constant of the substrate. The material systems found in this epitaxy are, i.e., AlAs/GaAs, AlP/GaP, etc. If the lattice-mismatched between two materials are highly different, the stress/strain in the system is induced. The strain in the system increases as the thickness of the strained layer increases. The effect of strain is explained in section 2.3.

In this thesis, the focus is aimed to use toward the lattice-mismatched material systems. All materials were GaAs [17], $In_xGa_{1-x}As$ [10], GaSb [18], and InSb [19]. As shown in table 2.1, the mentioned compounds are shown with their lattice constant, and their particular energy band at 300 K.

Table 2.1 Fundamental properties of GaAs, $In_xGa_{1-x}As$, GaSb, and InSb

Materials	Lattice Constant (Å)	Energy Gap (eV) at 300 K
GaAs	5.6533	1.42
GaSb	6.0959	0.68
InSb	6.479	0.17
$In_xGa_{1-x}As$	5.6533+0.405(x)	$0.324+0.7(1-x)+0.41(1-x)^2$

จุฬาลงกรณ์มหาวิทยาลัย
Chulalongkorn University

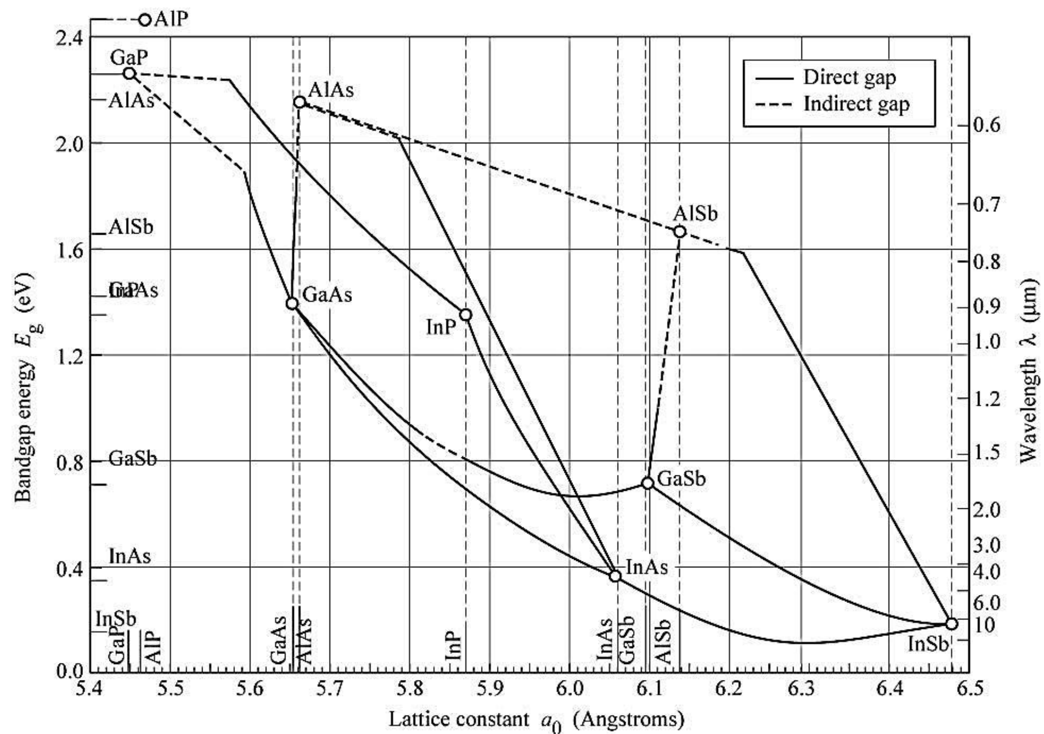

Figure 2.1 Energy gap and lattice constant of III-V compound semiconductors at room temperature.

จุฬาลงกรณ์มหาวิทยาลัย
Chulalongkorn University

2.3 Stress and Strain Relaxation

The existence of the stress in any material systems are mainly caused by the lattice-mismatched deposition. There are two types of strain, in general; (1) compressive strain and (2) tensile strain, as illustrated in figure 2.2. The deposition of GaSb or InSb or $In_xGa_{1-x}As$ onto GaAs yields the compressive strain which its stress accumulates as the thickness of deposition layer increases. When the increasing stress goes beyond the critical value (critical thickness), the strain relaxation is occurred. Thus, if accumulated strain in the system is high, some artifacts or island structures are formed. In contrast, if the accumulated strain in the system is considerably low, dislocation and surface step are possibly formed.

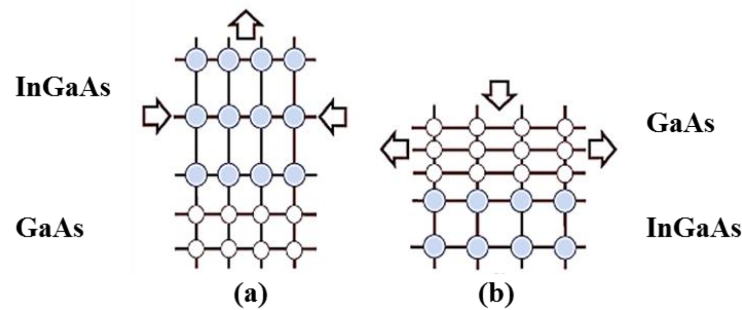

Figure 2.2 Diagram of (a) compressive strain and (b) tensile strain in InGaAs/GaAs system.

2.4 Dislocations and Surface Steps

Defect in the crystal can be categorized into four groups, which they are point defect, line defect, planar defect, and volume defect. The line defect is the initial imperfection, caused by incompletely bond of atoms at the interface. This line defect is also known as misfit dislocation (MD).

The MD at the material interface induces another dislocation, threading dislocation (TD), which forms in two directions. The first one is the TD that forms along [001]. This [001]-TD is known as pure edge dislocation. The second one is the TD that forms along <211> and lies incline 60˚ with the plane at interface [20]. The latter TD is a chain reaction of edge dislocation ($\mathbf{b}_{edge}$) and screw dislocation ($\mathbf{b}_{screw}$). The vector product between $\mathbf{b}_{edge}$ and $\mathbf{b}_{screw}$, shown id figure 2.3, is denoted as TD vector, **b**.

As proposed by M. Tamura *et al.*, [21] In molar fraction (x) that affect the TD is divided into three ranges. The first range is $x < 0.2$, the 60˚ dislocation is formed in this range. The second one is the range between 0.2 to 0.3, which the mixture between 60˚ dislocation and pure edge dislocation are formed. The last one is the range greater than 0.3, the TD found in this range are only the pure edge dislocation.

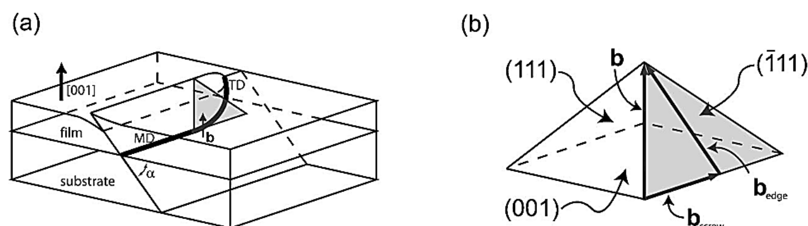

Figure 2.3 (a) Misfit and Threading dislocation that occur in heteroepitaxial deposition and (b) dislocation vector that occur from edge dislocation and screw dislocation [22].

There are two types of TD [23] generate at the material interface; (1) mobile TD and (2) immobile TD. Both types are considerably different in freedom of gliding. The immobile TD is blocked by the MD which is lying orthogonally to the TD, while the mobile TD can glide up through the film thickness toward the top surface [23]. The film surface becomes the surface steps lie orthogonal to each other along [1-10] and [110] direction. This surface configuration is also known as cross-hatch pattern (CHP). The CHP surface step elimination in CHP can be described as follows.

Figure 2.4 shows the surface step elimination [24] in CHP growth. Firstly, 2D film is deposited on the substrate where the strain is induced as the film thickness is growing thicker (see figure 2.4(a)). When the film thickness has reached its critical value, the surface steps are formed. These surface steps are affected from the slip planes in 60° dislocation, as shown in figure 2.4(b). Finally, the undulation surface is found after the overgrown layer is grown, as shown in figure 2.4(c).

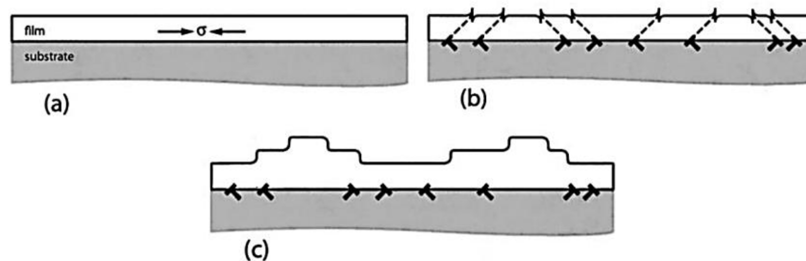

Figure 2.4 Surface step elimination process during CHP growth. (a) The accumulation of compressive strain in the 2D film. (b) Dislocation and surface steps at critical thickness. (c) Surface step elimination of overgrown layer [24].

2.5 Cross-Hatch Patterns

Cross-hatch pattern (CHP) can be found in many material systems, for example, InGaAs/GaAs [11, 25], GaAsP/GaAs [26], GaAs/Si [27, 28], SiGe/Si [29, 30], etc. CHP that have been developed and engineered [9, 31, 32] is a self-relieved strain due to the low lattice-mismatched (ε < 1.5) heteroepitaxy. The undulated patterns on the top surface are affected by the partial strain relaxation. In this thesis, InGaAs is grown on top of the GaAs to engineer the CHP template, and used for guiding antimonide QDs to align along the dislocation ridges.

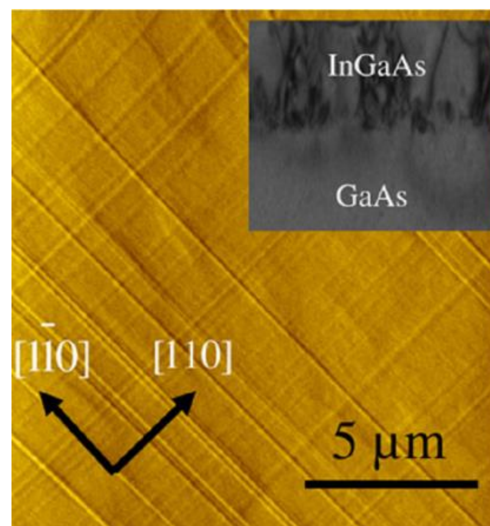

จุฬาลงกรณ์มหาวิทยาลัย
Chulalongkorn University

Figure 2.5 AFM image of cross-hatch pattern in InGaAs and GaAs [9].

The essential process for cross-hatch formation is the growth of $In_xGa_{1-x}As$ on GaAs, InGaAs is a stressor interacting on top of the GaAs layer. InGaAs is an alloy consists of three compositions among Indium, Gallium, and Arsenic. Its property plays an inter-role between the property of InAs and GaAs, which it is specified by the contents between Indium and Gallium. Thus, the general properties, for example, lattice constant and band energy can be adjustable.

2.5.1 Cross-Hatch Formation Mechanism

The deposition of InGaAs on GaAs [33] definitely form the compressive strain due to the lattice-mismatched. The existence of this strain is increases as the thickness of deposition layer is increased. The critical thickness of 60°-dislocation (h_{c60}) can be calculated by using set of Force Balance Model proposed by Matthews-Blakeslee model [34, 35]:

$$h_{c60} = \frac{\frac{G_{GaAs}G_{InGaAs}b}{\pi(G_{GaAs}+G_{InGaAs})(1-\nu)}(1-\nu(\cos\theta)^2)(\ln(\frac{h_{c60}}{b})+1)}{Yf} \tag{2.1}$$

$$G = C_{44} - \frac{1}{3}(2C_{44} + C_{12} - C_{11}) \tag{2.2}$$

$$b = \frac{\sqrt{2}}{2}a_{InGaAs} \tag{2.3}$$

$$\nu = \frac{C_{12}}{C_{21} + C_{11}} \tag{2.4}$$

$$Y = C_{11} + C_{12} - 2\frac{C_{12}^2}{C_{11}} \tag{2.5}$$

$$f = \frac{a_{InGaAs} - a_{GaAs}}{a_{InGaAs}} \tag{2.6}$$

where $\theta = 60°$, ν is Poisson ratio, G is anisotropic factor, C is elastic constant, amd Y is Young's modulus.

According to equation 2.1, assume that the clastic constant (C) is constant and linearly dependent to the In content in $In_xGa_{1-x}As$. The plot relation between In content and the critical thickness is shown in figure 2.6. We can see that, the critical thickness for $In_{0.17}Ga_{0.83}As$ is approximately 9 nm [36]. At this point, the elastic strain energy starts to saturate and partially relax the strain, and finally form the dislocations lines.

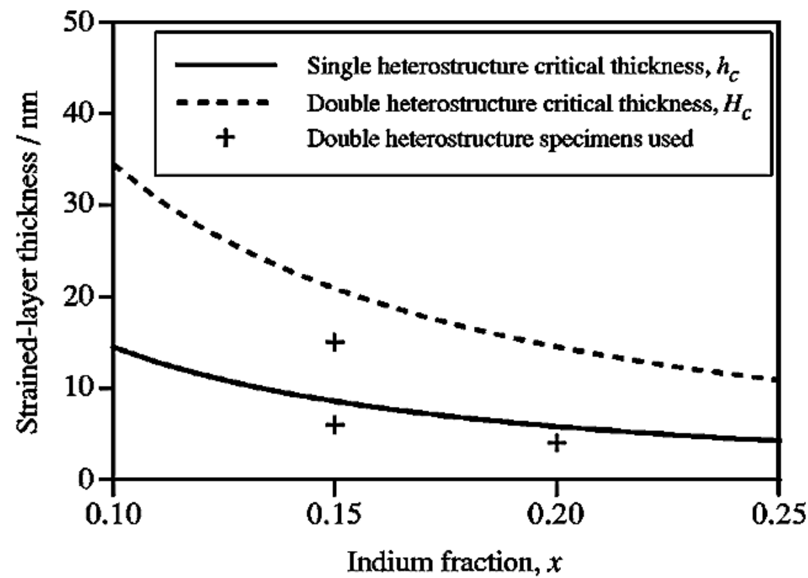

Figure 2.6 Critical thickness of 60˚- dislocation (h_{c60}) and In content of $In_xGa_{1-x}As$ [37].

2.6 Island Formation Mechanisms

The different nano-structures (1D, 2D, and 3D) yields from different growth modes. Each growth modes are classified by (1) lattice-mismatched (ε) in material systems, and (2) the layer thickness (H) [38].

The growth modes, shown in figure 2.7, comprise of six different growth modes. The details are provided as follows:

(1) **Frank-van de Merve Mode (FM)**; this mode occurs when the epitaxial layer is grown layer-by-layer. This growth mode is considered as a two-dimensional layer due to the lattice-mismatched in the system is less than 0.1 ($\varepsilon < 0.1$) and the grown layer is considerably a thin layer.

(2) **Volmer-Weber Mode (VW)**; this growth mode refers to the island growth. Since the laatice-mismatched of the material system is much greater than 0.1 ($\varepsilon > 0.1$), the deposited material are immediately relaxed and start forming island right away.

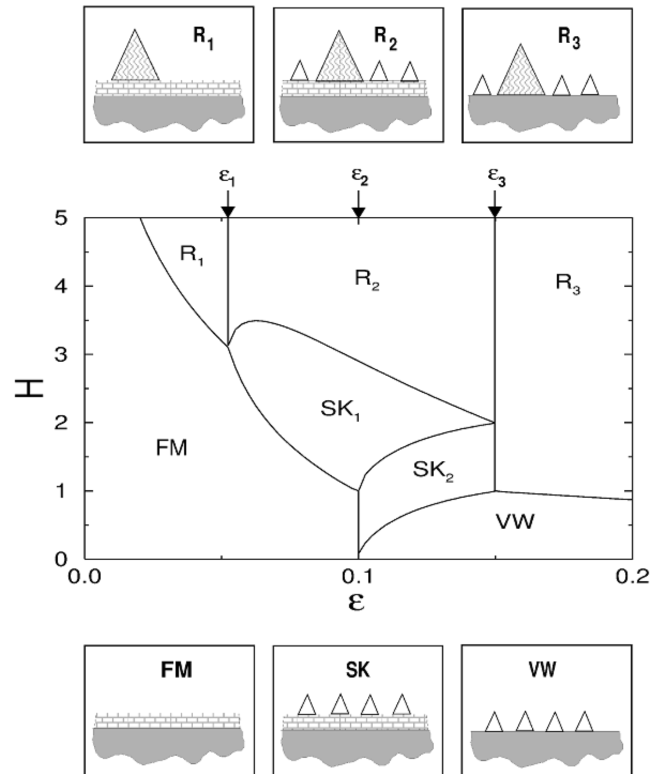

Figure 2.7 Equilibrium phase diagram of different growth modes as a function of H (layer thickness) and ε (strain). The first and last row images illustrate the nano-structures on the surface in different six growth modes. The small triangles represent the quasi-stable island and the large-shaded triangles represent the ripening islands. At the middle image, each limitation for each growth modes is drawn in their own boundaries as follows. $H_{c1}(\varepsilon)$: FM-R_1, FM-SK_1; $H_{C2}(\varepsilon)$: SK_1-R_2; $H_{C3}(\varepsilon)$: SK_2-SK_1; H_{C4} (ε) VW-SK_2, VW-R_3 [38].

CHULALONGKORN UNIVERSITY

(3) **Stanski-Krastranov Mode (SK)**; this mode occurs when the lattice-mismatched is moderately in the range between 0.05 to 0.15 ($0.05 < \varepsilon < 0.15$). The surface structures are found in combination between two-dimensional layer (FM mode) and three-dimensional island (VW mode). The SK mode can be classified into SK_1 and SK_2. SK_1 is the mode which the lattice-mismatched value lays close to that of FM mode. The formation starts from two-dimensional layer with the initiative of strain accumulation. This layer is called a wetting layer (WL). When the thickness of the epitaxial layer is increased, the accumulated strain in WL is relaxed and formed 3D islands.

On the other hand, in SK_2 mode, the initial stage of formation is 3D island because the lattice-mismatched value is close to VW mode. As the layer thickness is increased, the WL will be formed at the vacancy around the islands. However, the final stage between SK_1 and SK_2 are the same, only different in the formation mechanism.

(4) **R_1 mode**; The lattice-mismatched in this growth mode is less than 0.05 ($\varepsilon < 0.05$). It is a continuous mode from FM mode. The ripening island is formed on top of WL when the thickness of epitaxial layer (in FM mode) goes beyond the critical thickness ($H > H_c(\varepsilon)$).

(5) **R_2 mode**; The lattice-mismatched of this mode are in the range between 0.05 and 0.15. This formation mode is initialized from the SK mode, which the island can be fully formed (ripening islands) on WL. Moreover, some small islands are also found localized around the ripening islands.

(6) **R_3 mode**; The lattice-mismatched in this growth mode is less than 0.15 ($\varepsilon < 0.15$). It is a continuous mode from VW mode. The ripening island is formed among the small islands. None of the WL is found in this mode.

2.7 Low-Dimensional Nanostructure: Quantum Dots

When the size of the matter reaches down to the order of De Broglie wavelength, the carriers in its matter, generally electrons, behave as a wave-like particles due to the wave-particle duality in Quantum mechanics. The De Broglie wavelength is a relationship between momentum of the particle, $\boldsymbol{p}$, and the wavelength of particular wave-like particle, $\lambda_{DeBrogile}$, which can be written as [39],

$$\lambda_{DeBrogile} = \frac{h}{p} = \frac{h}{\sqrt{3m_{eff}k_bT}} \tag{2.7}$$

where h is Plank's constant, m_{eff} is a carrier effective mass, T is temperature and k_B is Boltzmann's constant. As the electron is considered as a carrier, De Broglie wavelength is yielded in nanometer scale.

There are three main classes of material dimensionality where they can specify the degree of freedom of the carriers. As illustrated in figure 2.8, the dimensional reduction of the structures –from bulk to quantum well, quantum wire, and quantum dot, leads to carrier localization in all directions.

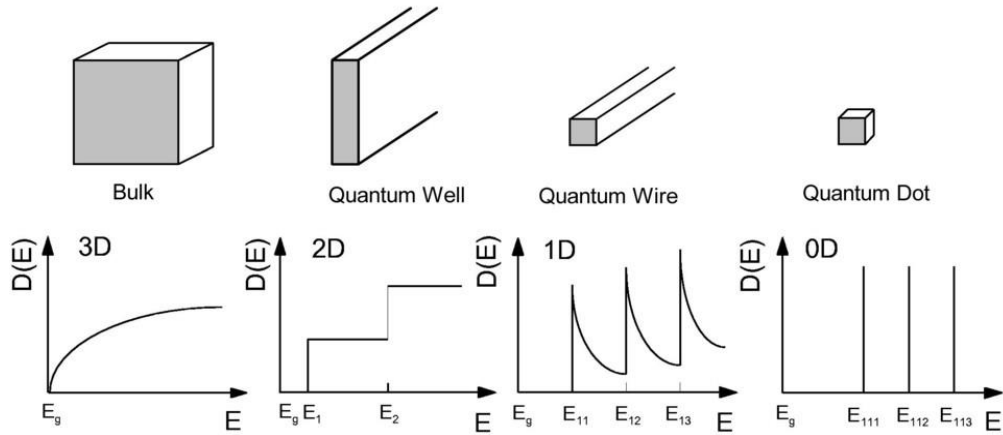

Figure 2.8 Schematic views and density of states (DOS) of (a) bulk, (b) quantum wells, (c) quantum wires and (d) Quantum dots [40].

Quantum dot is a nano-scale structure where the carriers are confined in all directions. The degree of freedom is said to be a quasi-zero. The density of state of quantum dot (D_{QD}), which is the number of states between the energy range E and $E+dE$. It can be written as,

$$D_{QD}(E) = 2N_D \sum_{n_x,n_y,n_z} \delta(E - E_{n_x} - E_{n_y} - E_{n_z}) \tag{2.8}$$

where N_D is the volume density of quantum dot and δ is delta function.

By solving Schrödinger equation for electron-wave function in infinite confinement potential barrier [40], we get

$$E_{QD} = E_{n_x} + E_{n_y} + E_{n_z} = \frac{\hbar^2}{2m^*}\left[\left(\frac{n_x\pi}{L_x}\right)^2 + \left(\frac{n_y\pi}{L_y}\right)^2 + \left(\frac{n_z\pi}{L_z}\right)^2\right] \tag{2.9}$$

where m^* is electron effective mass in conduction band, L_x, L_y, L_z are the length of infinite barrier along *x-*, *y-*, and *z-axis*, respectively, and n_x, n_y, n_z are principal quantum number.

As we can see from the mathematic solution for density of state, quantum dot has a discretized energy state which is represented by delta function. As we can see from the mathematic solution for density of state, quantum dot has a discretized energy state which is represented by delta function. This unique property leads to the narrow emission spectrum from QDs, while the bulk structure emits the broad spectrum. There are some studies demonstrating semiconductor laser-based QDs which consumes low-threshold current in operation [41]. However, the electrical and optical properties are tunable by engineering physical aspects of QDs such as size, alignment, etc.

จุฬาลงกรณ์มหาวิทยาลัย
Chulalongkorn University

CHAPTER 3
FABRICATIONS AND CHARACTERIZATION TECHNIQUES

The details of samples fabrication and characterization techniques are reported in this chapter. All the samples are fabricated by Molecular Beam Epitaxy (MBE) RIBER COMPACT-21T. The external installation of Sb cracker is used to supply Sb flux in antimonide QDs growth. The temperature calibration, growth rate calibration, and observing surface transition are monitored real time by *in situ* RHEED observation. The grown structures, i.e. CHP and QDs are characterized by AFM.

3.1 Molecular Beam Epitaxy

Molecular Beam Epitaxy (MBE) is an ultra-high vacuum (~10^{-11} Torr) based technique for epitaxial growth [42, 43] via the interaction of one or more molecular or atomic beams. This interaction occurs on a surface of a heated crystalline substrate. The ultra-pure elements are heated in separate effusion cells (i.e. Ga and As) until they begin to slowly sublimate. The evaporated atoms do not interact with each other until they reach at the substrate. The composition and the crystalline quality depend on the growth parameters and growth conditions, for example, beam flux and growth temperature, etc.

จุฬาลงกรณ์มหาวิทยาลัย
CHULALONGKORN UNIVERSITY

The advantages found in the MBE system are as follows [44]. (1) Sample surface preparation can be done by thermal cleaning under ultra-high vacuum condition. (2) The surface structure can be monitored real time by RHEED pattern, which the details will be described in the next section. (3) The controllable of crystalline film quality. At the ultra-high vacuum condition, some undesired gases such as H_2O, O_2, CO, and CO_2 do not present in the system. So that the contamination from those residual gases are not affecting the high quality deposited film.

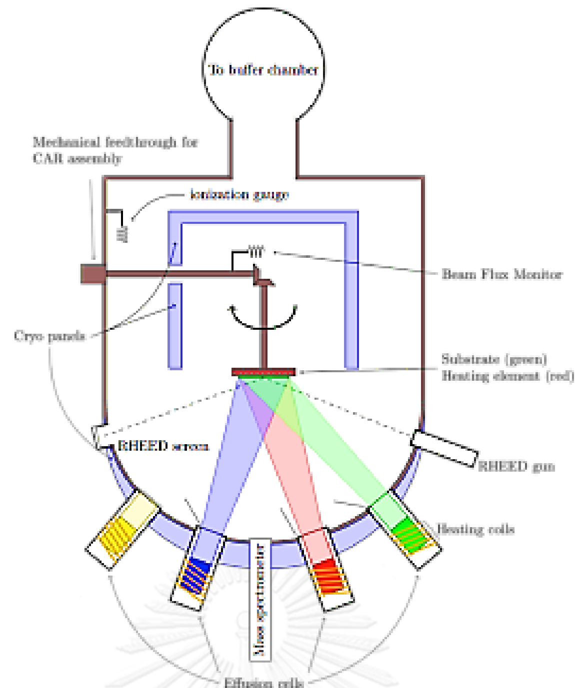

Figure 3.1 Cross-sectional diagram of the growth chamber in MBE system. The main components are effusion cells, RHEED system and gauge flux measurement.

All the growth procedures are run in the growth chamber. The cryopanel is an open-panel inside the growth chamber where liquid nitrogen (LN_2) is fed through the open-panel during the growth to cool down the chamber from heat transfer from heated effusion cells. The components in the growth chamber are manipulator, gauge flux, heater (for controlling substrate temperature), and RHEED systems as shown in figure 3.1.

As shown in figure 3.2, the MBE chamber, RIBER Comapact-21T, is the machine that has been used for QDs fabrications for the entire experiments in this thesis.

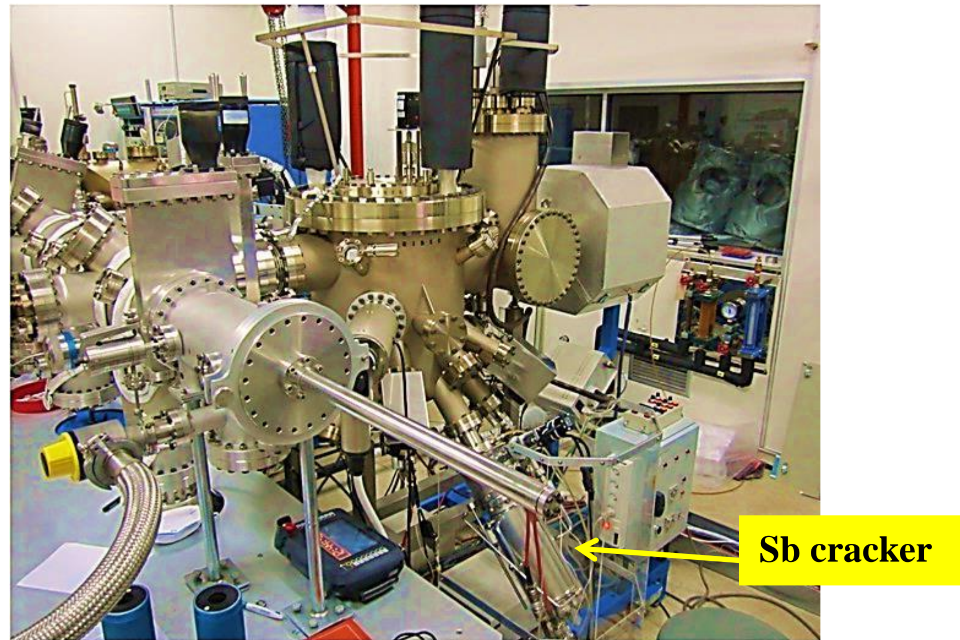

Figure 3.2 Molecular Beam Epitaxy, RIBER Compact-21T with an external Sb cracker installation.

3.2 Reflection High Energy Electron Diffraction

Reflection High Energy Electron Diffraction (RHEED) is an important *in situ* monitoring technique. It is used to analyze and specify the surface structure. The reflected electron beam manifests the patterns that confirm, for example, the smoothness, and nanostructure on the surface. The patterns from RHEED depend on the atomic arrangement on the substrate. When the high-energy electron beam form the electron gun is exposed onto the material surface at a small angle (~1˚- 2˚), the electron beam diffracted out of the surface structure and reveals the patterns on phosphorus screen. The different structures on the surface reflect the diffraction of the electron beam in different patterns. Schematic of RHEED system is shown figure 3.3.

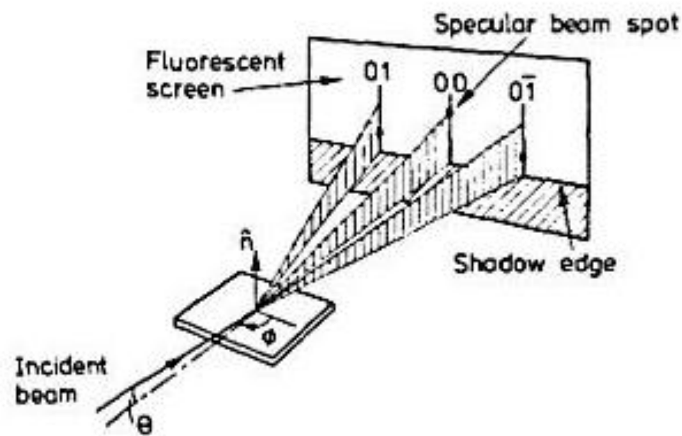

Figure 3.3 Schematic diagram of RHEED geometry. The elongated spots indicate the intersection of the Ewald sphere with the (01), (00), and (0-1) rods.

The observed RHEED patterns on phosphorus screen is the pattern construction based on Laue diffraction condition [45] which is found to be a reciprocal lattice space image. As shown in figure 3.4(a), streaky pattern indicates the smooth and flat surfaces. When three-dimensional islands or rough surface form on the surface, the RHEED pattern becomes the spotty patterns (see figure 3.4(b)). Moreover, RHEED intensity oscillation can be applied for substrate temperature and growth rate calibrations. These advantages of RHEED oscillation will be described in details in section 3.4.2, and 3.4.3, respectively.

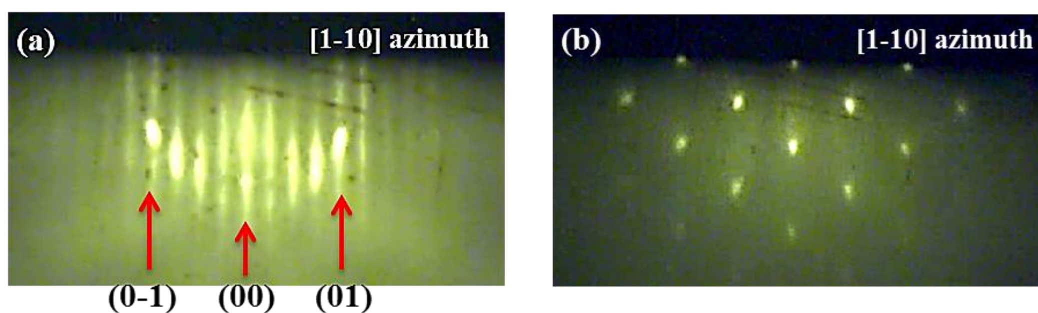

Figure 3.4 (a) Streaky pattern, and (b) spotty pattern.

3.3 Pre-Fabrication Processes

This section explains in details about sample preparation. The sub-processes are (1) substrate pre-heating, (2) oxide-desorption, (3) temperature calibration, and (4) growth rate calibration.

3.3.1 Sample Preparation

After the substrate is well-mounted onto the Molybdenum block (Mo-block) by melted Indium, the Mo-block is then transferred into the transfer chamber before transferring to the pre-heat chamber. The thermal preheating process started off by heating the Mo-block to approximately 450˚C with the ramp rate of 30˚C/min. Then, the substrate is dwell at that temperature for about one hour before the program automatically ramps the substrate temperature down to around room temperature. The temperature profile for pre-heating process is illustrated in figure 3.5. According to substrate pre-heating process, some water, oxide, and other gas that loosely bonded on the surface (protective oxide) are removed out of the substrate surface and trapped by the ion-pump inside the pre-heat chamber.

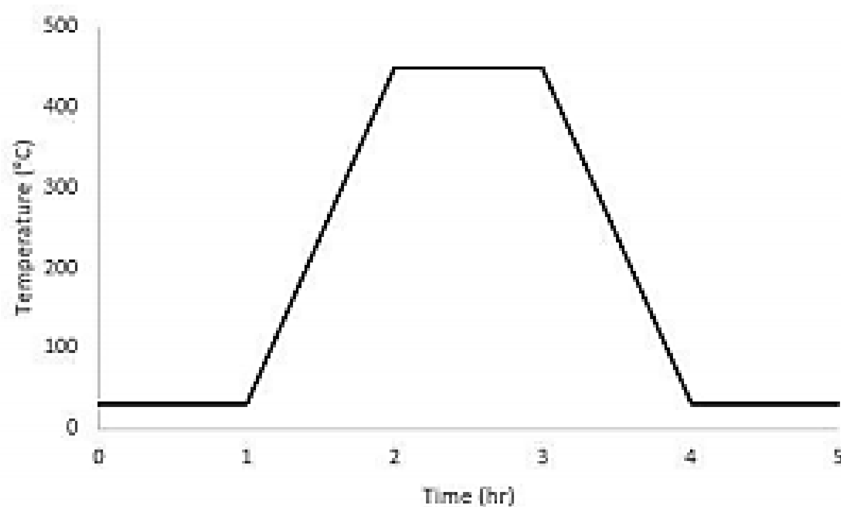

Figure 3.5 Temperature profile for pre-heating process.

Consequently, the Mo-block is transferred into the growth chamber where the liquid nitrogen is feeding through all the time during the growth run. Oxide desorption is a process that is done to remove the native-oxide attaching on the surface [43]. Form this process onward, the RHEED pattern is observed to monitor the real time surface construction for the entire growth run. Prior to the process, the Mo-block is heated up to 580˚C to 600˚C and dwell at this temperature for about ten minutes in the presences of As beam (4.0×10^{-6} Torr to 1.0×10^{-5} Torr). Note that, this step must be done in the atmosphere of group-V otherwise the substrate surface would be damaged by thermally decomposing [43]. The substrate surface reveals the atomically clean GaAs surface when the streaky RHEED pattern is shown up on the phosphorus screen. The temperature at the time when the streaky pattern appears is indicated as 580˚C for the growth of GaAs buffer. At 580˚C, 100-nm GaAs buffer layer was deposited onto the substrate for the following temperature calibration.

3.3.2 Temperature Calibration

Substrate heating plays an important role in MBE growth since it provides the proper energy for atom to mobile on the growth interface to ensure that the growth proceeds epitaxially. And also has a direct influence on all the other kinetic process [43]. Due to the temperature read by thermocouple is not a real temperature that presents on the substrate surface. To do so, the temperature measurement is needed to perform. The change of substrate temperature is causing the atomic reconstruction on the surface and more reliable to use as a reference value.

In practical, firstly, the THEED pattern must be adjusted showing the (2×4) pattern which is found in [1-10] azimuth. The substrate temperature is decreased until the RHEED pattern changes from (2×4) to *c*(4×4). Next, the substrate temperature is ramped up again to 580˚C. During the increasing of substrate temperature, the RHEED pattern changes again from *c*(4×4) to (2×4). The temperatures at which the RHEED patterns change are noted as T_1, T_2, T_3, and T_4. The average temperature of those four temperatures is defined as 500˚C, which refers to the appropriate temperature for surface reconstruction. The changes of the RHEED pattern during the substrate temperature calibration are shown in figure 3.6.

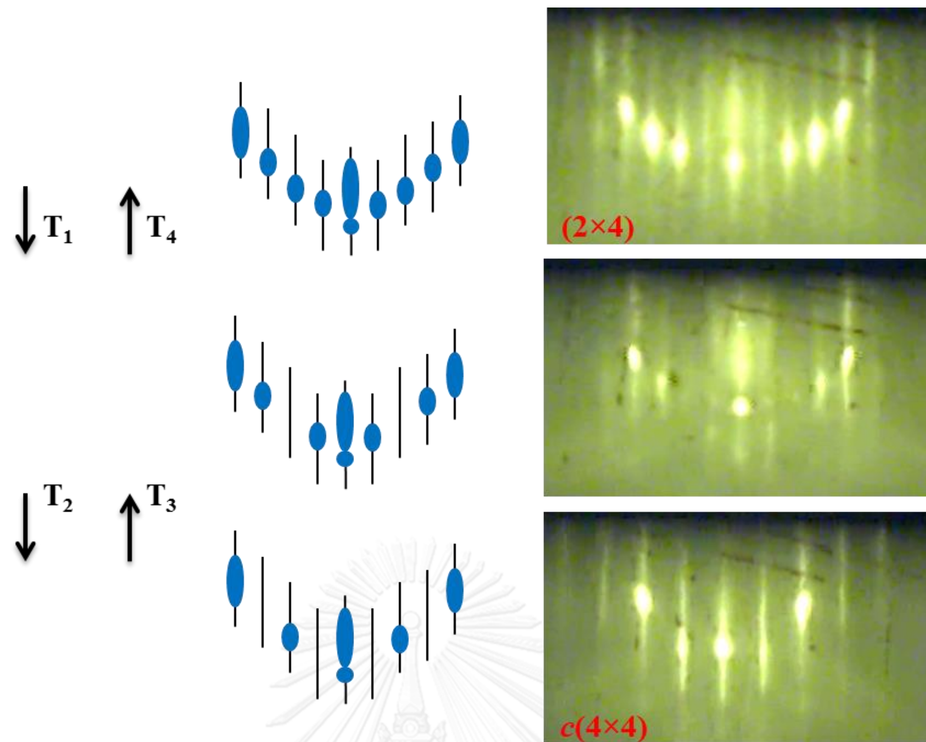

Figure 3.6 Schematic diagram of [1-10] azimuth RHEED pattern transition during temperature calibration process.

3.3.3 Growth-Rate Calibration

Growth rate is one of the crucial parameter which is used to specify the thickness of the deposition layer, and content of the materials in ternary and quaternary compounds. The amount of flux is dependent to the cell temperature before opening shutter. By taking advantage on RHEED intensity oscillation, the growth rate of GaAs, and InAs are calibrated to define the Ga and In contents, respectively for $In_{0.17}Ga_{0.83}As$ CHP. The details of growth rate calibration for each compound are explained in the following sections.

3.3.3.1 Growth-Rate Calibration for GaAs

For GaAs growth rate calibration, GaAs layer will be deposited layer-by-layer on the substrate. First of all, be sure that the substrate surface is completely flat by observing the streaky RHEED pattern on the phosphorus screen. Next, the Ga cell is heated to the temperature that relates to the designated Ga flux. Then, stop rotating manipulator and adjust the RHEED pattern to observe the [1-10]- azimuth. After that, Ga shutter is opened to grow GaAs layer. At the specular beam on RHEED pattern (00), its intensity oscillates from high intensity to low intensity. This changes according to the fraction of surface coverage as clarified in figure 3.7. The maximum-minimum intensity oscillation in one cycle is equivalent to the GaAs deposition for one monolayer (ML).

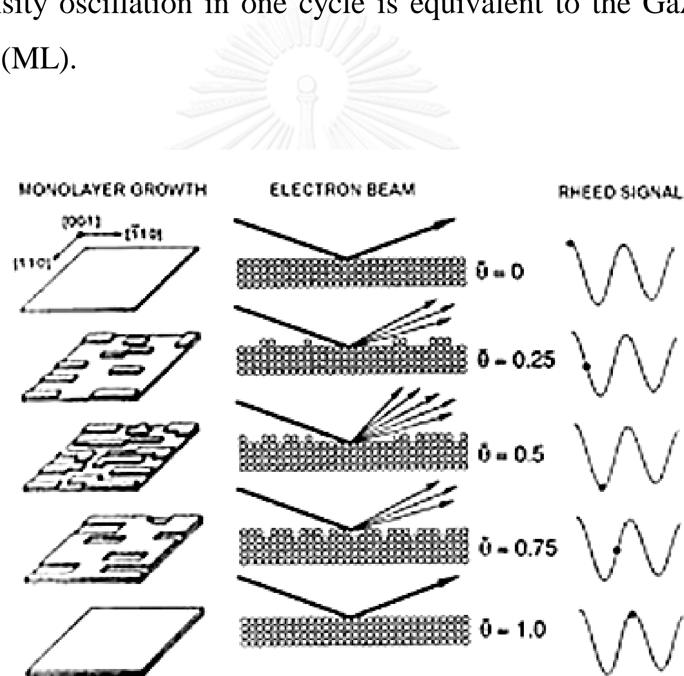

Figure 3.7 (a) two-dimensional GaAs layer formation on GaAs (001) [46].

Figure 3.8 shows the real specular beam intensity oscillation that is monitored during the GaAs growth rate calibration at 500˚C. According to the figure, three oscillation peaks are lap during GaAs deposition. This three laps equivalent to 3 ML for GaAs layer. When the number of oscillation cycle is divided by the time consuming for those particular cycles, then the Ga growth rate in ML/s is obtained.

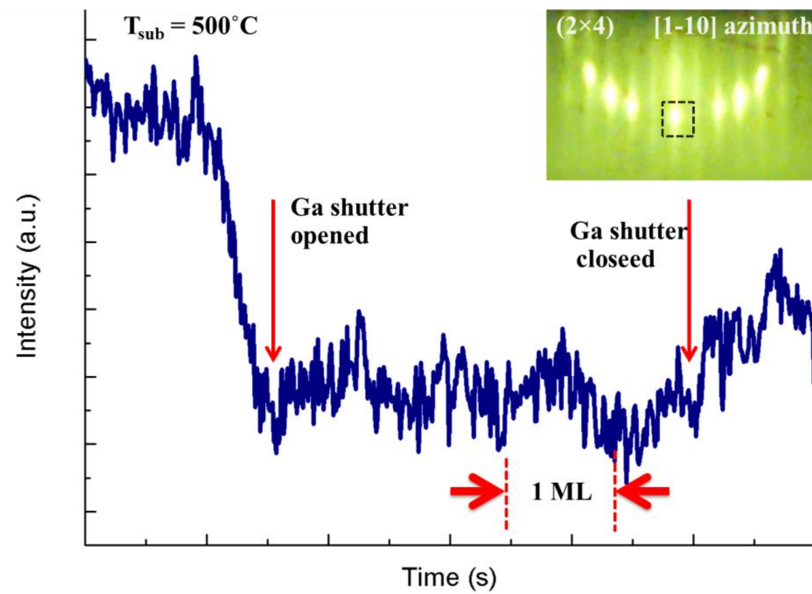

Figure 3.8 RHEED intensity oscillation of GaAs taken in this experiment. Square box in inset image indicates the specular beam spot that used for intensity observation.

3.3.3.2 Growth-Rate Calibration for InAs

InAs growth rate calibration procedure is different from GaAs. Since InAs is lattice-mismatched to GaAs, the surface construction is not a layer any longer and yet forms the thee-dimensional island. The critical thickness for InAs film before forming the islands is ~1.7 ML. At this thickness, the RHEED pattern changes from streaky to spotty is revealed. To do the InAs calibration, the In cell is heated to the temperature that relates to the In flux. Then, In shutter is opened for InAs deposition at 500˚C. In-shutter is closed abruptly after the RHEED pattern shows the spotty pattern. The time taken for island formation is lap for growth rate calculation as well. The division between InAs thickness, 1.7 ML, and time taken for island formation is equivalent to the deposition rate for InAs. Finally, the Mo-block must be ramped up to the oxide desorption temperature in order to desorb InAs QDs before re-growing GaAs buffer to flatten the roughness surface caused by InAs QDs formation.

3.3.4 GaAs Buffer Deposition

Buffer layer is a crystalline film of GaAs. It was grown to prepare smooth surface before performing the growth in following the layers. The growth of GaAs buffer layer is done at the substrate temperature of 580˚C by opening Ga shutter under As_4 atmosphere with the GaAs growth rate of ~0.5 ML/s. In this experiment, the total thickness of GaAs buffer layer is 400 nm.

3.4 Fabrication Processes

3.4.1 CHP and GaAs Spacer

The 30-nm $In_{0.17}Ga_{0.83}As$ cross-hatch pattern (CHP), with the indium content of 17%, is fixed as a template for all QDs growth. In order to growth CHP, the growth rate of InAs and GaAs are calibrated to be ~0.04 ML/s and ~0.2 ML/s, respectively to get the In content of 17%. This content is determined from growth rate relation [47] between two alloy compounds as:

$$x = \frac{\Phi(InAs)}{\Phi(InAs) + \Phi(GaAs)} \tag{3.1}$$

where x is In content, $\Phi(InAs)$ and $\Phi(GaAs)$ are the growth rate of InAs and GaAs, respectively.

At the substrate temperature of 500˚C, the In and Ga shutters are opened simultaneously to deposit both beams onto the substrate. In, Ga, and As_4 interact with each other on the surface to construct the $In_xGa_{1-x}As$ layer. It should be noted that, if the In content exceeds 20%, the roughness surface can easily form due to the high (>1.5) lattice-mismatched to the GaAs layer. This roughness is confirmed by spotty RHEED pattern.

After the growth of InGaAs layer, the 6-nm GaAs spacer is introduced over InGaAs layer with the GaAs growth rate of ~0.2 ML/s. The reason for the GaAs spacer growth is to (1) smooth out the epitaxial surface and (2) to reduce the

จุฬาลงกรณ์มหาวิทยาลัย
Chulalongkorn University

compressive strain caused by lattice-mismatched in InGaAs/GaAs material system. By growing GaAs spacer, we believe that the tensile strain in GaAs/InGaAs/GaAs system would create un-strained surface at the flat area, while the CHP ridges are still experiences the compressive strain as depicted in figure 3.9.

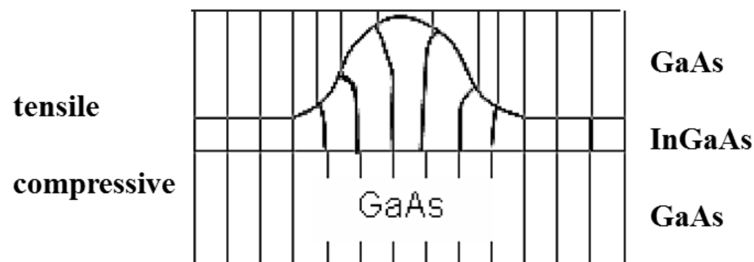

Figure 3.9 Schematic of strained GaAs/InGaAs/GaAs system.

3.4.2 Quantum Dots Growth

GaSb and InSb QDs are grown on CHP. The substrate temperature for GaSb QDs formation is 500˚C while the substrate temperature for InSb QDs formation is 300˚C. In order to grow antimonide QDs, the As_4 atoms are stopped supplying prior to clean out the chamber from As and to reduce the anion, As-Sb, intermixing rate as much as possible. The growth chamber is ready for antimonide QDs growth when the background pressure reached down below 5.0×10^{-9} Torr. The growth rate of GaAs and InAs are used at ~0.08-0.1 ML/s, and ~0.01 ML/s, respectively. In addition, two different growth techniques are performed in QDs formation; conventional method, and migration enhance epitaxy (MEE).

3.4.2.1 Conventional Method

For conventional growth technique, Sb beam is supplied onto the substrate surface for one minute before opening group-III shutter. The group-III shutter is abruptly closed right after the spotty RHEED pattern is constructed. After that, the growth interruption is introduced for one minute under Sb beam for atomic arrangement. Finally, the substrate temperature is decreased to 100˚C to freeze the QDs structures.

3.4.2.2 Migration Enhance Epitaxy

For migration enhance epitaxy growth technique, the shutter between group-III and Sb-cracker valve are set to respond in different time sequent [48, 49]. The main shutters sequent in one duty cycle used in this experiment comprises of 20 s for Sb soaking, *t* s for group-III atoms deposition, and 5 s for growth interruption. Note that *t* refers to the exposing time for group-III beam. The exposing time for each antimonide QDs growth, GaSb and InSb, could be seen in experimental results of chapter 4. When the formation of QDs which confirms by RHEED transition from streaky-to-spotty pattern, the growth process is kept running until the shutters duty cycle completes. Figure 3.10 shows the comparison of shutters sequence between conventional growth and migration enhance epitaxy.

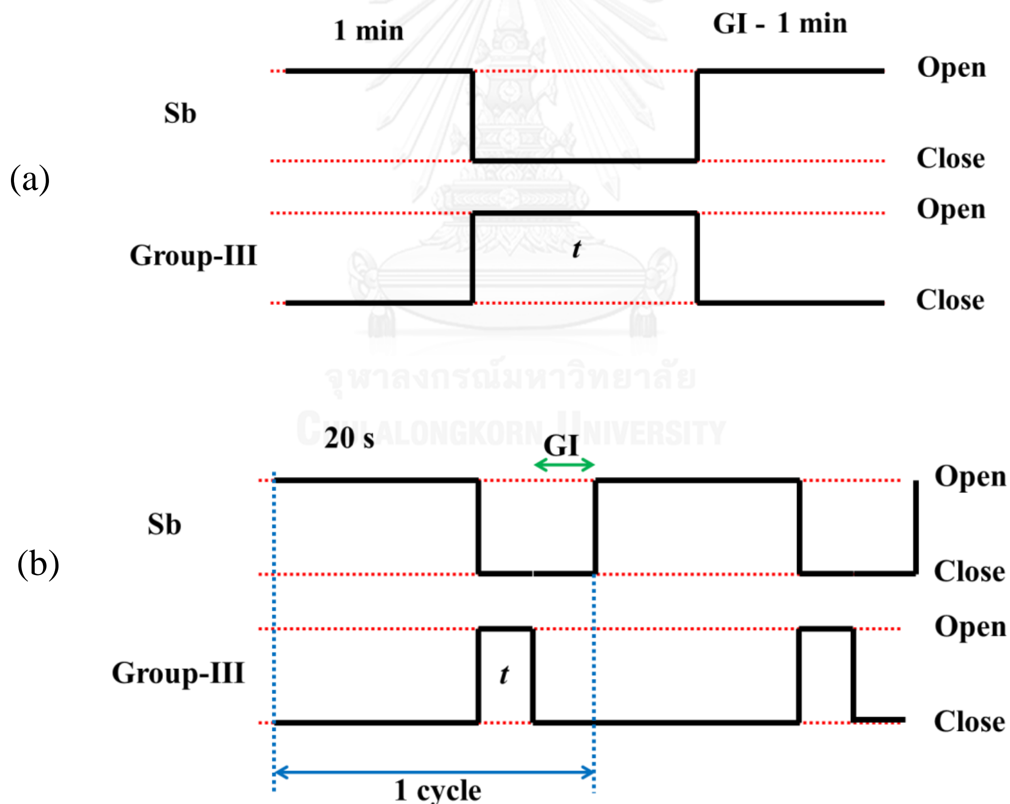

Figure 3.10 Shutter sequence of Sb and group-III atoms in antimonide QDs growth by (a) conventional method, and (b) migration enhance epitaxy.

3.4.3 GaAs Capping Layer

The capping layer is the coverage layer where the surface state caused by the dangling bonds exists. When the carriers in the material transport to this stage, a non-radiative recombination is occurred. So, GaAs capping layer is grown to reduce the effect from surface state [50]. In this experiment, the capping layer is grown for 100 nm with two step growth. The first step, 40-nm GaAs layer is grown at low temperature and the second step, 60-nm GaAs is grown at high temperature. The growth details and rationales for each step are provided in chapter 4.

3.5 Post-Growth Characterizations

Ex situ characterizations, such as morphology and optical property, are carried out after the growth. The main simple characterization machines in crystal growth are atomic force microscopy, and photoluminescence set-up.

3.5.1 Atomic Force Microscopy

Atomic force microscopy (AFM) is a tool that has been used for nano-scale morphology characterization. The main information that can be extracted from the AFM are, i.e., size distribution, nano-structural shape, density, and height distribution, etc.

จุฬาลงกรณ์มหาวิทยาลัย
Chulalongkorn University

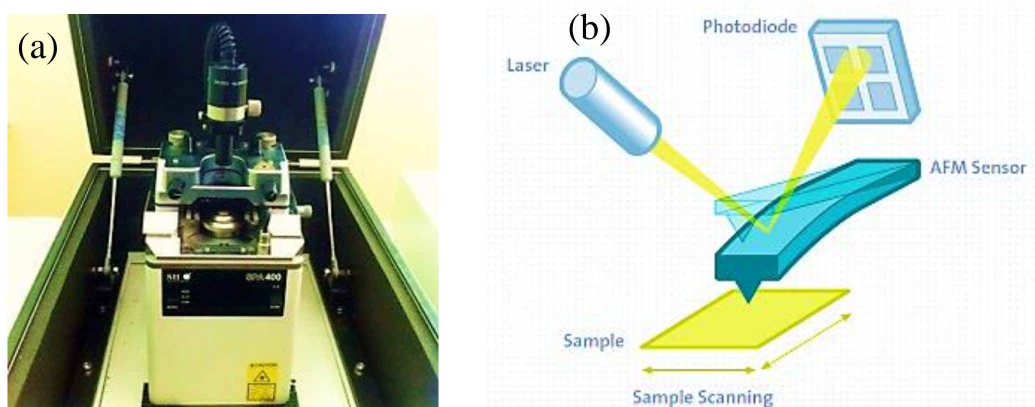

Figure 3.11 (a) Atomic force microscopy (AFM), and (b) systematic diagram of AFM.

There are three working modes that have been used in AFM. Those three modes are (1) contact mode, (2) tapping mode, and (3) non-contact mode. The latter mode, non-contact mode, is the working mode that widely used in semiconductor morphology characterization since it is a non-destructive method. We can considerably sure that the material surface would not be destroyed. Figure 3.11(a) shows the AFM machine, Seiko (SPA-400), that has been used for the topology characterization.

The basic principle of AFM is the making use of Van Der Waals force between the probe tip and semiconductor surface. The AFM components consist of probe tip, laser and laser detector. As shown in figure 3.11(b), when a piezo-electric stage moves the sample toward a scanning direction, the tip experiences the height contrast at each position on the topological surface while the Van Der Waals force keeps the distance apart between the tip and the surface. The tip oscillation due to the different height on the surface reflects the changing of optical path length that point geometrically on the tip to the laser detector. The detector, then, converts the detected signals to the topological profile.

3.5.2 Photoluminescence

The excitation laser used in this experiment is a 519-nm Ar^+ laser. First of all, the laser beam is chopped by a chopper for generating the pulse-like beam from a continuous beam. The chopping frequency is 330 Hz prior to reduce electrical noise generated from 50-Hz power supply. Then, the laser will be focused onto a sample, which is mounted in cryostat under the vacuum condition. The emitted photons will be collected and focused to a monochrometer where the light signals are resolved by the grating inside monochrometer. Finally, the resolved light is detected by liquid N_2-cooled InGaAs detector and is amplified by a lock-in amplifier. The optical apparatus set-up is shown in figure 3.12.

จุฬาลงกรณ์มหาวิทยาลัย
CHULALONGKORN UNIVERSITY

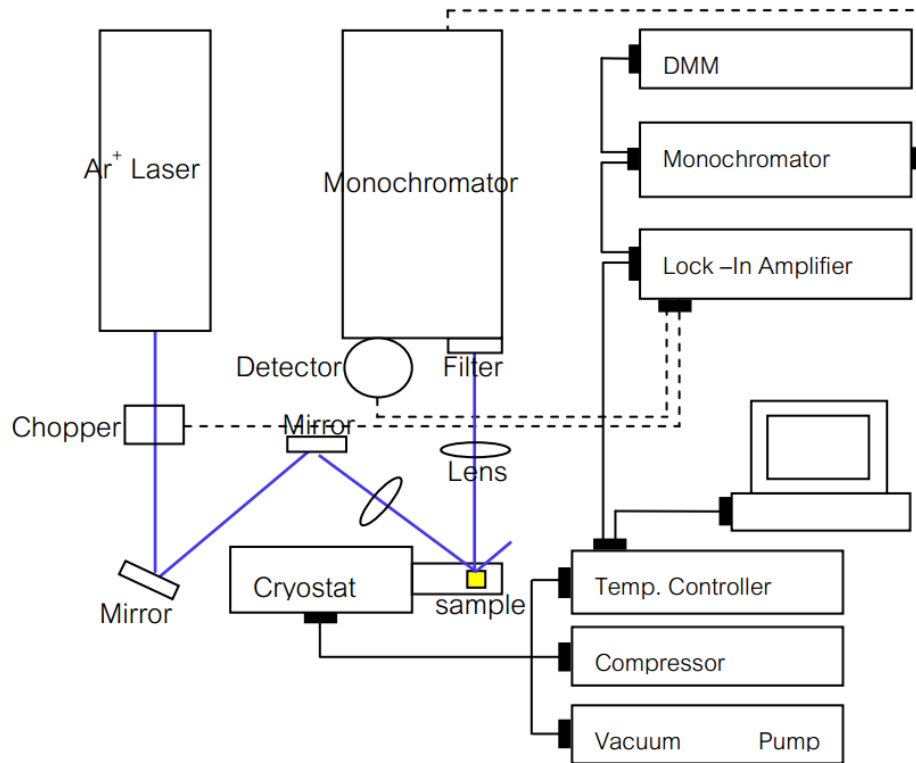

Figure 3.12 Experimental set-up diagram of photoluminescence measurement.

จุฬาลงกรณ์มหาวิทยาลัย
Chulalongkorn University

CHAPTER 4
GaSb AND InSb ON CROSS-HATCH PATTERNS

The main focus for this thesis is to study the effect of strain, relieved from partial relaxation of cross-hatch patterns (CHP), to the guidance of antimonide QDs formation. The results are divided into four main parts. The first part, section 4.1, is the sample details for CHP template. Section 4.2 presents the optimization results for CHP template which the nominal thickness of InGaAs layer, narrow width of undulated ridges, and low density ridges are obtained. The third and the last sections report the morphologies and optical properties of GaSb and InSb QDs, respectively. The size distribution of antimonide QDs grown by different growth techniques-conventional and MEE methods- are compared. Finally, the mechanism on strain-guided antimonide QDs formation is clarified.

4.1 CHP Growth Details

After thin native oxides have been removed from the GaAs (001) surface by heating the substrate to the temperature of about 600˚C in the presences of As_4, atomically clean GaAs surface is obtained. Next, the substrate surface is flattened out by GaAs buffer layer for 400 nm at 580˚C. Then, the substrate temperature is decreased to 500˚C for growing InGaAs cross-hatch patterns (CHP). At this step, the In and Ga shutters are open simultaneously with InAs growth rate of ~0.04 ML/s and GaAs growth rate of ~0.2 ML/s to obtain *d*-nm $In_{0.17}Ga_{0.83}As$ CHP, where *d* is the thickness and will be optimized as explained in section 4.2. The growth interruption is performed for 30 seconds before and after the deposition of 6-nm GaAs spacer. The structural diagram of CHP includes the temperature details are depicted in figure 4.1. After that, the temperature of the As cell is reduced to keep the chamber out of As_4 atoms. Performing antimonide quantum dots (QDs) growth would be done when the background pressure drops to 5.0×10^{-9} Torr. In order to study the nucleation GaSb

and InSb QDs, the growth is set to the condition as explained in sections 4.3 and 4.4, respectively.

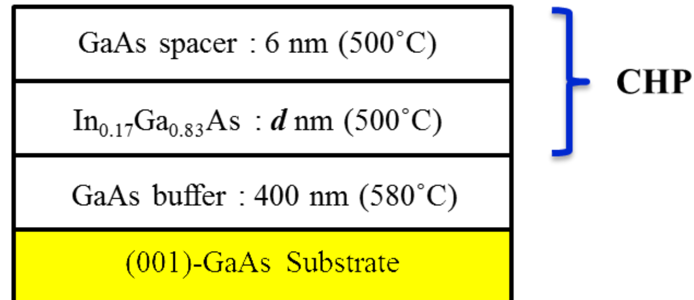

Figure 4.1 Schematic diagram of the CHP structure. ***d*** is the InGaAs thickness.

4.2 Optimizing CHP Template

The main purpose for this section is to report the optimization of InGaAs cross-hatch patterns (CHP). According to the study presented by Barabási *et al.* (1997) [51], the strain energy distribution of the island structure was calculated by two-dimensional atomistic model. The result shows the existence of minimum strain energy at the top-most position on the island while the strain energy at the edges have a maximum value and rapidly decreases along the position far from the island. The modified figure of the strain distribution is shown in figure 4.2.

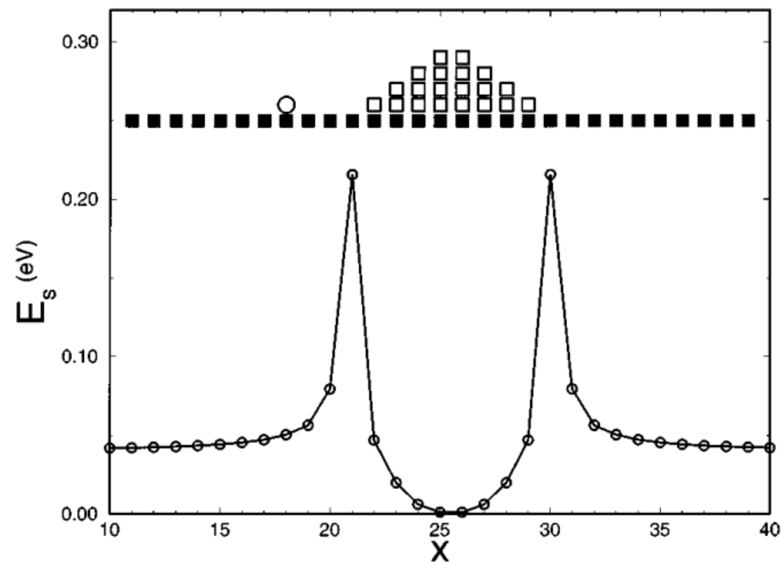

Figure 4.2 The schematic diagram of strain energy distribution in a function of position of one-dimensional island. The filled and empty squares are represented the atoms of substrate and the island [51].

Another calculation in strain energy distribution using atomistic model by E. Penev *et al.* (2001) revealed that islands with different widths have different strain energy distributions. As depicted in figure 4.3, the narrower width of island presents a narrow strain distribution, $\varepsilon(x)$. Also, the narrow width of island gives the highest different between the strain energy values at the island edge and the top-most position of the island when compare to the case of wider island width. In the latter observation, the steeper strain energy serves as a potential barrier for adatoms localization.

Based upon the calculation results by Barabási *et al.* (1997) and E. Penev *et al*. (2001), the CHP were optimized to obtain appropriate pattern for studying the strained-guidance effect as follows. (1) The surface is desired to have low-density ridges so that flat area dominates. This condition helps in judging how the CHP strain field influences the adatoms accumulation and island formation. (2) The narrow width of the ridges is desired to get the steep strain gradient. This condition ensures the high energy barrier that blocks migrating atoms.

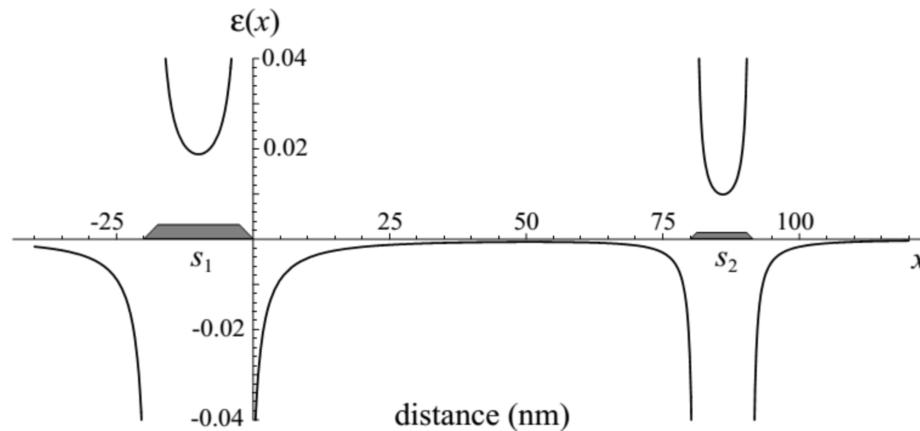

Figure 4.3 The schematic diagram of strain field, $\varepsilon(x)$, of two one-dimensional islands with different island width, s_1 and s_2 which s_2 is smaller than s_1. The two islands are separated by a distance L much greater than s_1 and s_2 [52].

The main parameter in controlling the size and ridge distribution is the *thickness of CHP*. In this experiment, the thickness of CHP with the Indium-mole fraction of 17% was varied from 25 nm to 40 nm. This range of thickness is greater than the critical thickness, h_c, of CHP which for $In_{0.17}Ga_{0.83}As$ is ~9 nm [34]. *Ex situ* characterization by atomic force microscope (AFM) shows the surface undulation of CHP. The ridges found in all AFM images appear along the [1-10]- and [110]-crystallographic directions which are orthogonal to each other. The [1-10] ridges dominate since the glide velocity of the α-dislocation is higher than the β-dislocation along [110] in InGaAs ternary system [53]. According to the figure 4.4, as the CHP thickness increases, number of misfit dislocations (ridges) also increases. When the number of ridges increases, they occur closer to each other and tend to merge forming stripes. This resulting in barrier height reduction and strain distribution broadening. In contrast, the shallower CHP layer thickness gives a very low density ridges and narrower ridges width as shown in figure 4.4 (b).

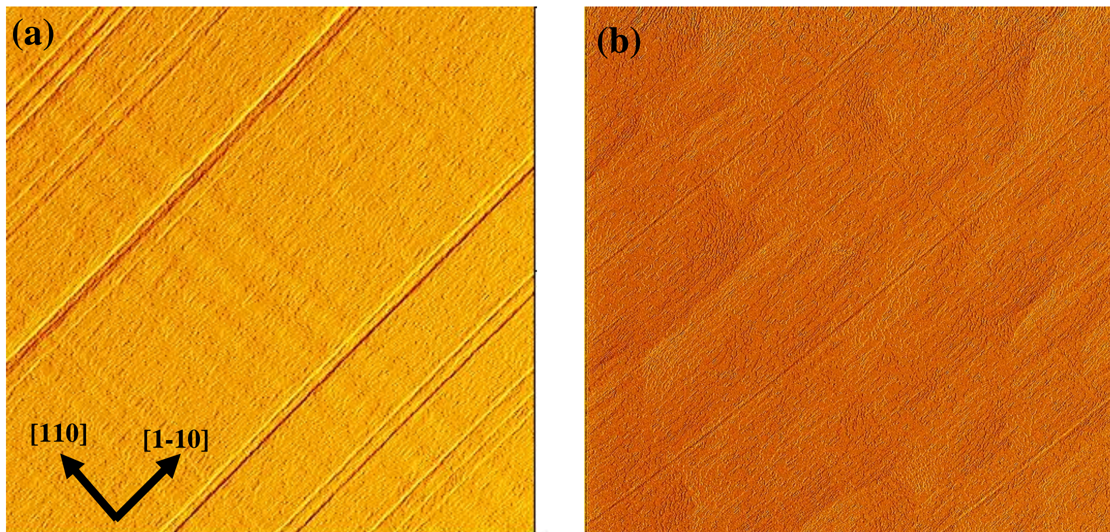

Figure 4.4 10×10 μm^2 AFM images of CHP with thickness of (a) 40 nm, and (b) 30 nm, respectively.

Eventually, the 30-nm $In_{0.17}Ga_{0.83}As$ with a 6-nm GaAs spacer layer on top serves as a CHP template and reproduces for GaSb and InSb QDs growth prior to the study strain-guided island nucleation. The structural diagram includes the temperature detail of CHP is depicted in figure 4.5.

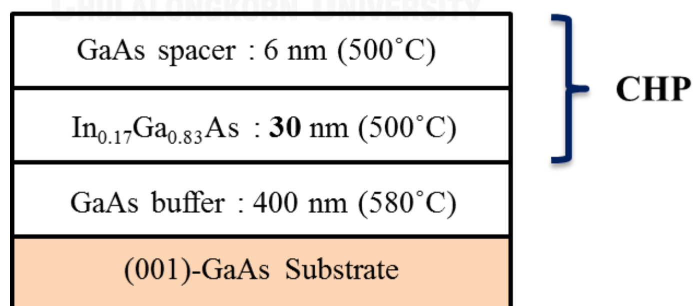

Figure 4.5 Cross-sectional CHP template for antomonide QDs growth. The optimal CHP thickness is 30 nm.

4.3 GaSb on CHP Grown by Conventional and MEE Methods

This section presents the realization of GaSb QDs formation underlying the growth parameters such as temperature and growth techniques; (1) MBE, conventional method and (2) MEE, migration enhance epitaxy.

4.3.1 Morphology

In this experiment, the growth of GaSb QDs on CHP is set into two conditions as clarified in table 1. In both conditions, GaSb QDs are grown at substrate temperature of 500˚C and the Gallium growth rate is ~0.08 ML/s to ~0.1 ML/s. For the first condition, GaSb QDs in the sample 1 is grown by using MBE conventional technique which both Sb-cracker valve and Ga shutter are open simultaneously. The growth interruption is also performed for one minute under Sb atmosphere for atomic arrangement to their steady state condition. Another condition is to grow by migration enhance epitaxy (MEE). MEE is a technique that cell-shutters between group-III and group-V elements are open at different time sequences. For sample 2, the shutter sequence in one cycle consists of 20 s-Sb, 1 s-Ga, and 5 s-growth interruption. Both growth conditions are stop (for conventional method)/ completed cycles (for MEE) when the spotty RHEED pattern appears.

จุฬาลงกรณ์มหาวิทยาลัย
Chulalongkorn University

Table 4.1 Growth condition for GaSb QDs on CHP

GaSb QDs	Sample 1	Sample 2
Growth temperature	500˚C	500˚C
Growth technique	MBE	MEE: 1 cycle= (20s-Sb, 1s-Ga, 5s-GI)

*GI = Growth interruption under neither group-III nor –V atoms are supplied.

Figure 4.6 shows the 5×5 μm^2 AFM images of GaSb QDs grown on CHP template by performing two different deposition techniques: (1) Conventional method (MBE), and (2) Migration Enhance Epitaxy (MEE). According to figure 4.6 (a), there are some GaSb QDs align along the CHP ridges in both [1-10]- and [110]- crystallographic directions among the free-standing GaSb QDs, which distribute all over the flat area. This can be occurred due to the nature of Sb atom that has high sticking coefficient and manifests low diffusibility [54]. When Ga adatoms are deposited onto the template surface where the supplied Sb atoms are diffusing around, they interact with each other before bonding with another atomic site on the surface.

In the case of GaSb QDs grown on CHP by MEE, the result is different. Due to the supplementary materials between Ga and Sb atoms are deposited on the substrate surface in sequences; Ga and Sb are supplied at different time, we can make use of this advantage to enhance the diffusion length of group-III adatoms. The less disturbance of Sb atoms (small number of Sb atoms on the surface) to the Ga adatoms leads to the possibility for Ga adatoms to diffuse further on the surface until they find preferentially site to coalesce with. As the coalesced GaSb layer thickness increases beyond its critical thickness, the strain relaxes and consequently forms the GaSb islands. It seems that GaSb QDs preferentially nucleate at the top-most area along the cross-hatch ridge, as shown in figure 4.6(c). Moreover, the nucleation of GaSb QDs is also found dominantly along the [1-10]- crystallographic sites.

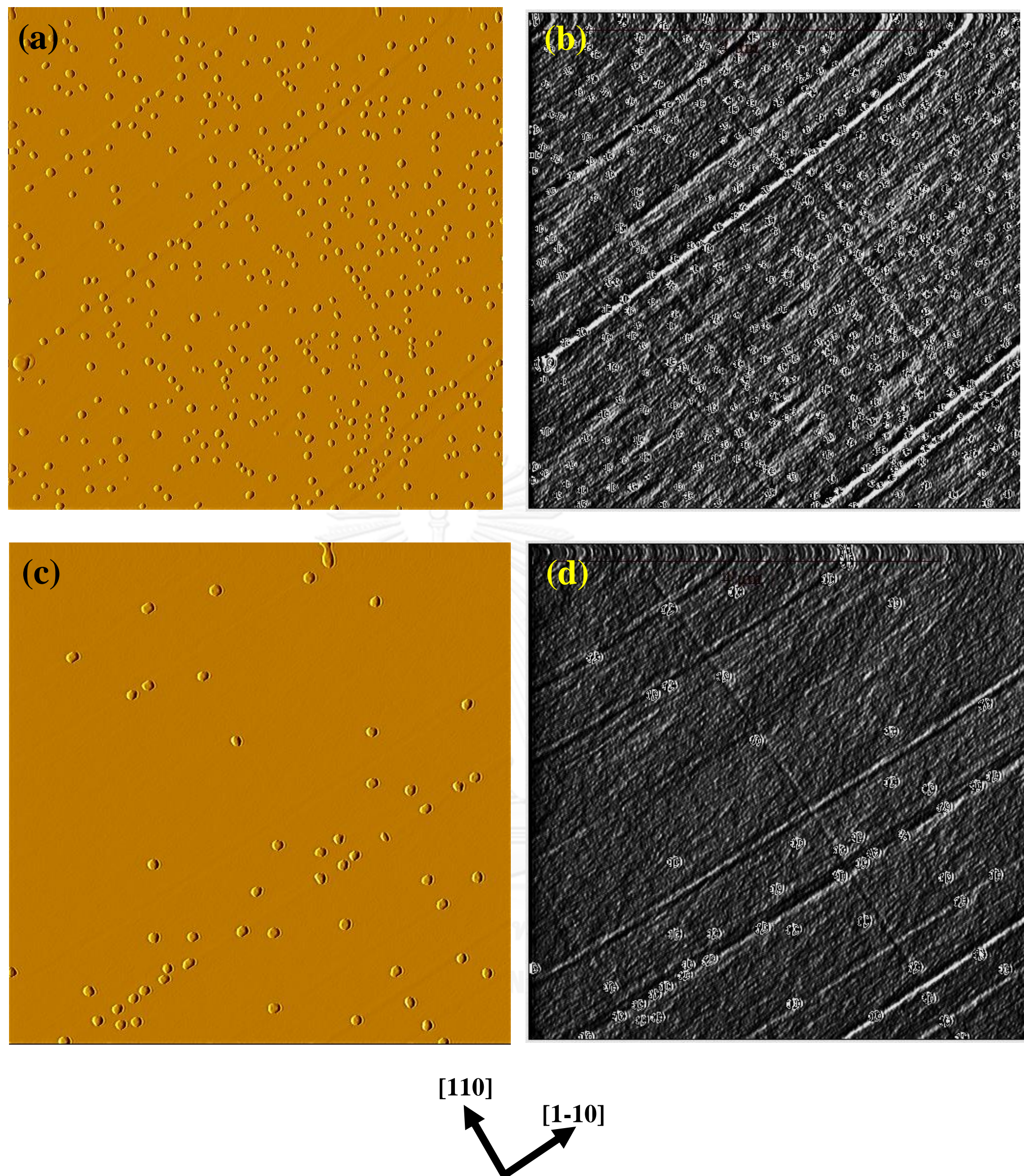

Figure 4.6 (a) and (b) are the 5×5 μm^2 AFM images of GaSb QDs, grown by MBE technique, shown in NC force and height field image mode, respectively. (c) and (d) are 5×5 μm^2 AFM images, grown by MEE technique, shown in NC force and height field image mode, respectively.

Figures 4.6(b) and 4.6(d) illustrate the height contrast image. The CHP ridges along both [1-10]- and [110]- directions that are hidden away from the AFM images are revealed. The output images also clarify that the [1-10]- ridges are more dominant than the ridges found along [110]- direction. This information is obtained by an image processing built-in command in Gwydions [55]. The original image is filtered out by a standardized kernel matrix. After the convolution process, the height contrast image is obtained.

To conclude on the effect of the strain- guided GaSb QDs formation, the kinetic aspects together with MEE growth technique have to be taken into account. Figure 4.7 illustrates the mechanism for the nucleation of GaSb QDs grown by MEE technique. The explanation on each step is given as follows:

(1) Ga adatom is deposited onto the CHP surface, at which the elastic strain energy at the ridge experiences a steep strain gradient.
(2) By applying MEE technique, of which the reduction of Sb atoms enhances the Ga adatom to migrate further on the surface. Cooperation with the surface energy provided by thermal activation energy and long diffusibility of Ga adatom, it is able to overcome the high strain energy position of the CHP's edge. They, Ga-Sb molecules, then start settling down at the topmost area on CHP where the minimum strain energy presents.
(3) Existing Ga-Sb molecules along the CHP makes the strain energy at the particular area (along the ridges) shallower [52]. This might be a crucial process that induces another molecules hoping up from the edge easily before bonding with the pre-existing atoms.
(4) Accordingly, the accumulation of Ga-Sb molecules on CHP increases a strained GaSb layer until the stress energy relaxation occurs to form a GaSb QD.

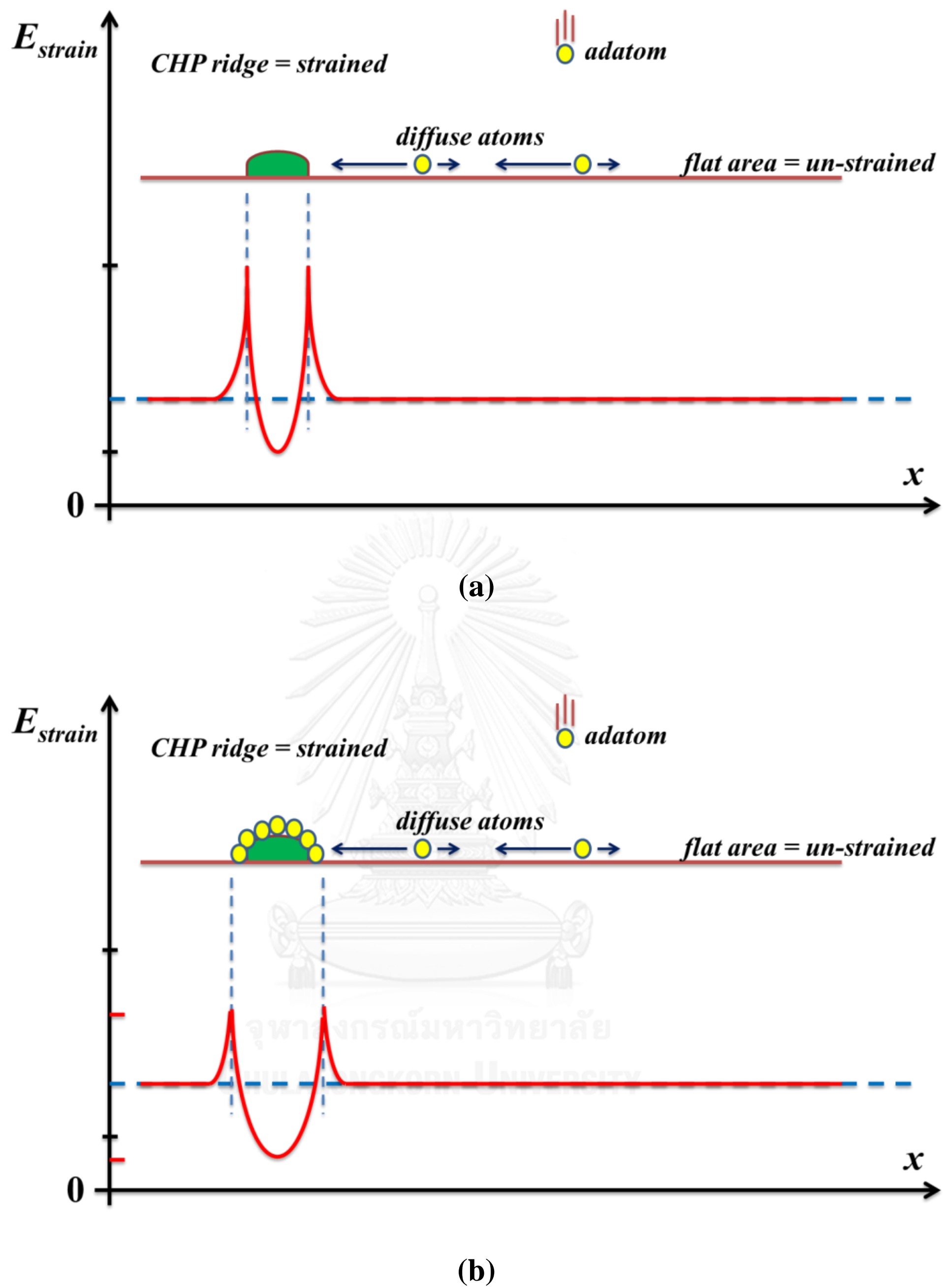

Figure 4.7 Illustration diagrams of the mechanism of GaSb QDs formation, grown by MEE technique, on a CHP ridge. (a) and (b) are the images show the before and after nucleation.

4.3.2 Size Distribution

The GaSb QDs that we measured the height are the QDs that the Ga adatoms are stop depositing immediately (for conventional method)/ completed shutters duty cycle (for MEE) right after the RHEED oscillation reveals the 2D-to-3D surface transformation. Along with this constrain, we could answer the question that *where is the primitive area, strained or un-strained sites, that GaSb QDs preferentially nucleate*.

First comparison case, the height distribution of GaSb QDs which forms on flat area and CHP ridges obtained from the conventional growth method are compared. The average height of GaSb QDs that nucleate along the CHP ridges is around 13.3 ± 2.6 nm which is greater than that of free-standing GaSb QDs, which is around 11.8 ± 1.8 nm.

In the same way, the height distributions of GaSb QDs that forms along the CHP ridges obtained from different growth techniques are compared. The comparison shows that the average height of GaSb QDs grown by MEE is almost double that of GaSb QDs grown by conventional technique. Their mean values are 20.3 ± 2.9 nm and 13.3 ± 2.6 nm, respectively. The mean height for each comparison cases are summarized in table 4.2 and the histograms of height distribution in each case can be found in figure 4.8.

CHULALONGKORN UNIVERSITY

Table 4.2 Average height of GaSb QDs

	Average Height (nm)	
	Conventional Method	**MEE Method**
CHP ridges	13.3 ± 2.6 nm	20.3 ± 2.9 nm
Flat area	11.8 ± 1.8 nm	-

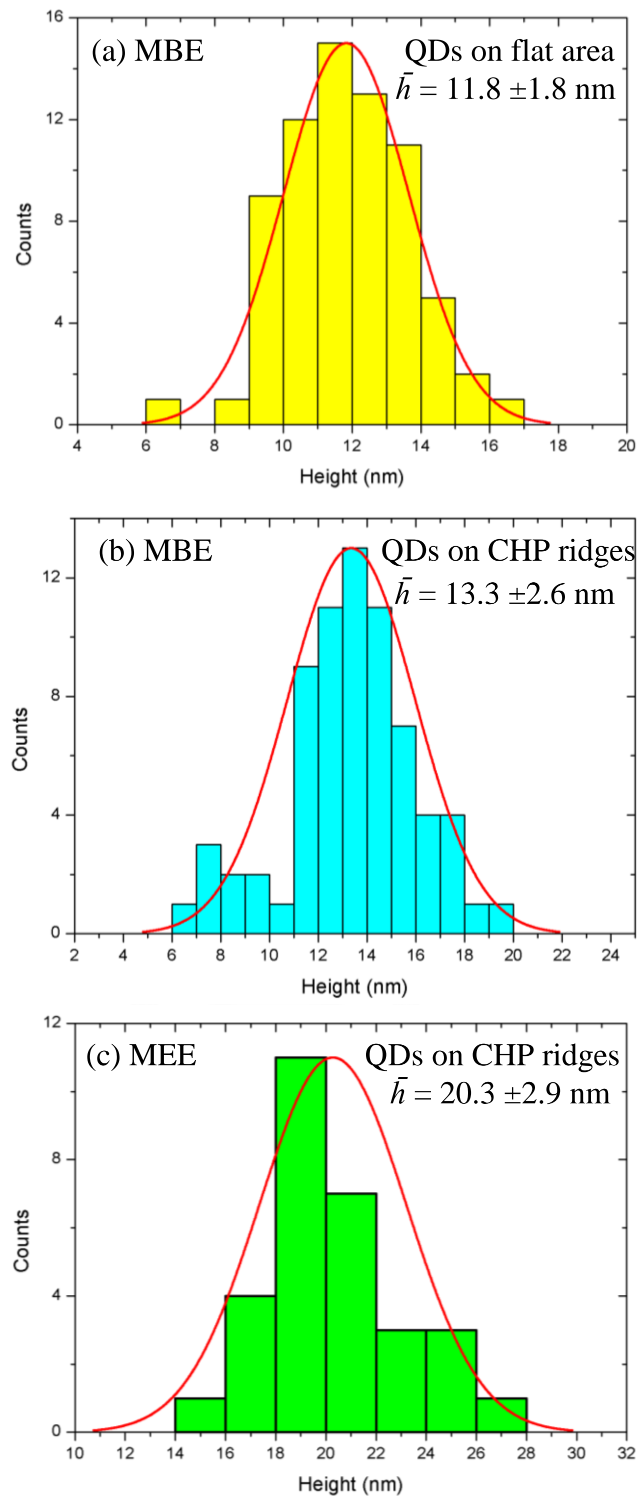

Figure 4.8 Histogram of height distribution of GaSb QDs grown by conventional method, (a) and (b), and MEE method (c). The size distribution was measured on (a) flat area, and (c), (d) along CHP ridges. The Gaussian curve fit and the center position of the Gaussian peak are shown in the figures.

The observation on height distribution agrees well with the nucleation theory in term of kinetic aspect; atoms preferentially migrate to the low strain energy area. Direct comparison on height distribution for GaSb QDs within the conventional growth technique itself shows a gradual different value, because that small difference value lies in the same range as the height of CHP ridges (approximately 1-2 nm). Nevertheless, the different in mean height is obviously seen when the modified growth technique, MEE, had performed. This technique enhances the migration length of group-III atoms by diminishing group-V atoms. So, this could answer that the compressive strain along CHP ridges can guide the accumulation of Ga-Sb atoms and finally form the islands.

Moreover, when we closely consider about the GaSb QDs shapes found in both samples, there are two main configurations found in the GaSb QDs on CHP.
The first configuration is the elongated shape of some QDs that form along the ridge. Their shapes tend to expand out along the direction where they localize at. For example, the QD shape on [1-10]-ridge elongates and fits its shape along [1-10]-direction. As shown in figure 4.9 (c) and (d), the line profiles of their shapes along [110]- and [1-10]-directions show a strong asymmetric configurations. While the line profile of QDs on flat areas show the symmetric configuration with the circular based shape. This effect would be claimed on the impact of strain energy can highly induce adatoms to accumulate along the strained sites. Figure 4.9 shows the existence of GaSb QDs shapes found in both samples.

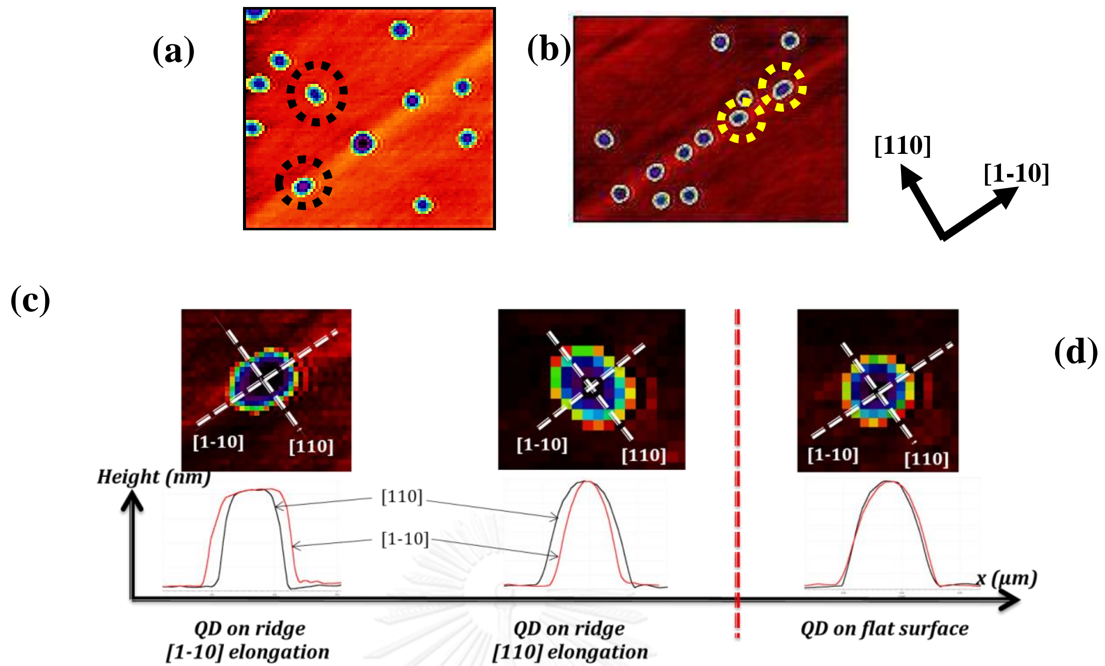

Figure 4.9 (a) and (b) are the selected area of AFM images of GaSb QDs, grown by MBE and MEE, respectively. The elongated GaSb QDs are highlighted in the dashed circles. (c) is the shape configurations of some QDs found on the CHP ridge and (d) is the shape configuration of most QDs found on flat area with their particular line profiles.

4.3.3 Optical Property of GaSb QDs on CHP

In order to study the optical property of GaSb QDs on CHP, the structure is grown by MEE technique with the shutters duty cycle of 20-s Sb, 3-s Ga, 5-s GI. We expect to obtain more GaSb QDs align along the CHP ridges. After the CHP template is grown, 100-nm GaAs capping layer was performed with two-step growth run. With the ~0.5 ML/s deposition rate for GaAs, the first step is the growth of 40-nm capping layer at 400˚C to prevent anion exchange [56]; consequently, another 60-nm GaAs is deposited onto the first capping layer at 500˚C. Finally, the GaSb QDs on CHP structure is re-grown to confirm the buried surface morphology.

Figure 4.10 shows the 5×5 μm^2 AFM image of the re-grown GaSb QDs on CHP which reveals the underneath GaSb QDs and the morphology confirms the alignment of GaSb QDs along the ridges and on the oval defects [57] (see arrows point in image of figure 4.10). The latter defect might come from the substrate over heating during the oxide-desorption process. However, this result confirms the guiding effect of strain/ defects to the island nucleation.

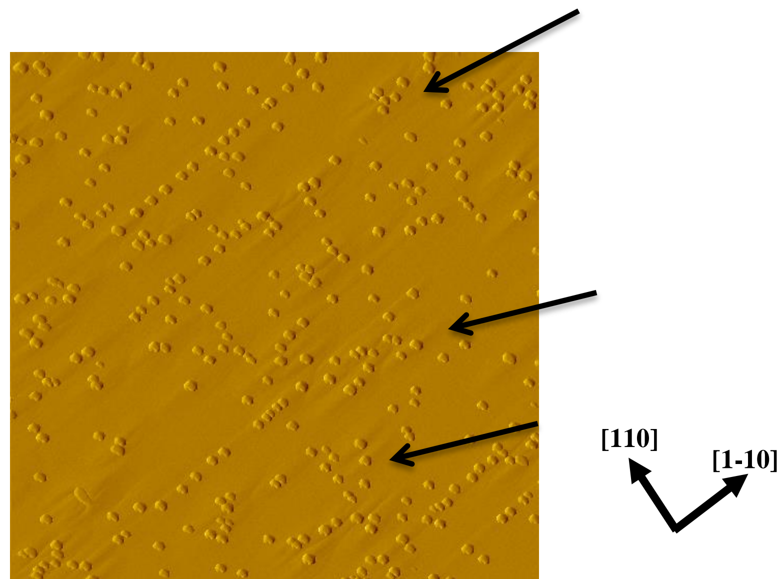

Figure 4.10 5×5 μm^2 AFM image of the re-grown GaSb QDs on CHP. The arrows indicate some oval defects.

จุฬาลงกรณ์มหาวิทยาลัย
Chulalongkorn University

Photoluminescence spectrum can be used to classify the PL energy peak whether the particular peaks are from the carrier recombination in ground state or excited state. In this PL observation, five laser powers ranging from 20 mW to 200 mW were exposed onto the sample at the temperature of 20 K. It should be noted that, the emitted photons are excited from the side-surface of the sample during the measurement. The increasing of laser power activates the carriers-filling state process [58], thus, it directly increases the intensity of responded spectrum.

According to the fundamental study on GaSb QDs grown on InGaAs on InP substrate [59], and GaSb QDs on GaAs layer [4], their morphologies was characterized and their optical properties were observed at low-temperature. Those results clarified their peaks of quantum structure which centered at ~0.75 eV in GaSb/InGaAs/InP system and at ~1.11 eV in GaSb/GaAs system. In addition, the material systems were confirmed to be type-II characteristic by observing the blue shift in power-dependent PL when the linearly dependent plot between Energy peaks and third root of excitation powers were observed.

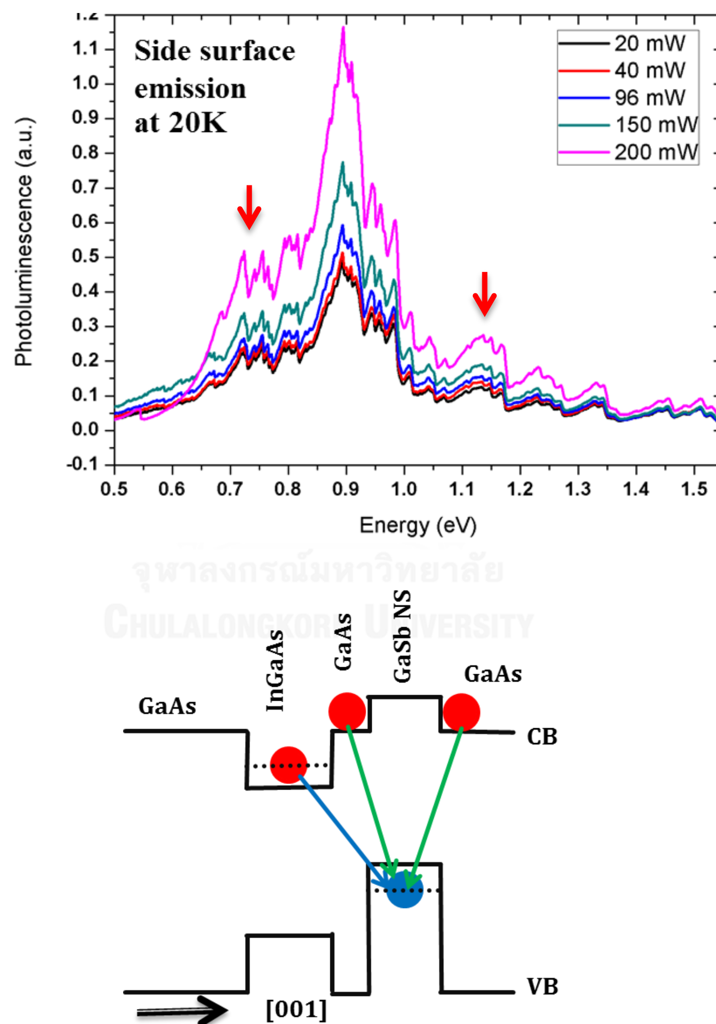

จุฬาลงกรณ์มหาวิทยาลัย
CHULALONGKORN UNIVERSITY

Figure 4.11(a) Power-dependent PL spectrum of GaSb QDs grown by MEE technique. The QD peaks are found at ~0.73-0.75 eV and ~1.14 eV as denote by the arrows. (b) is a schematic diagram of carriers transitions in GaSb QDs structure.

Based on our experimental set-up, two important QD peaks in the literatures [4, 59] match to the peaks found in this measurement. The first one is the peak at ~0.73-0.75 eV which is possible in carrier transition between GaSb QDs and InGaAs layer. Another peak is at ~1.14 eV which is possible in the carrier transition between QDs and GaAs layer.

On contrary, the energy peaks of GaSb/InGaAs and GaSb/GaAs are considered as type-II structure; the relation between cube root of excitation power and energy peak position are linearly dependent [4, 59]. But in this experiment we found no energy shift is observed. We believe that our PL apparatus and set-up should be optimized for the mid- and long- IR wavelength detection.

4.4 InSb on CHP

After the CHP is grown as explained in the first paragraph of section 4.1, the growth temperatures are optimized prior to figure out the suitable temperature for InSb QDs formation. In the experiments, the growth condition for InSb QDs on CHP is set as follows. Two samples are grown at different temperatures. One is grown at 400˚C, while the other one is grown at 300˚C. In order to grow InSb QDs, the entire chamber is soaked by Sb_4 for one minute and then In shutter with the InAs growth rate of ~0.014 ML/s is opened. In shutter is closed right after the streaky RHEED pattern turns to spotty pattern. Both samples are still kept at growth temperature under Sb atmosphere for one minute before freezing the structure. Their morphology was characterized by AFM.

จุฬาลงกรณ์มหาวิทยาลัย
CHULALONGKORN UNIVERSITY

4.4.1 Morphology: Effect of Growth Temperatures

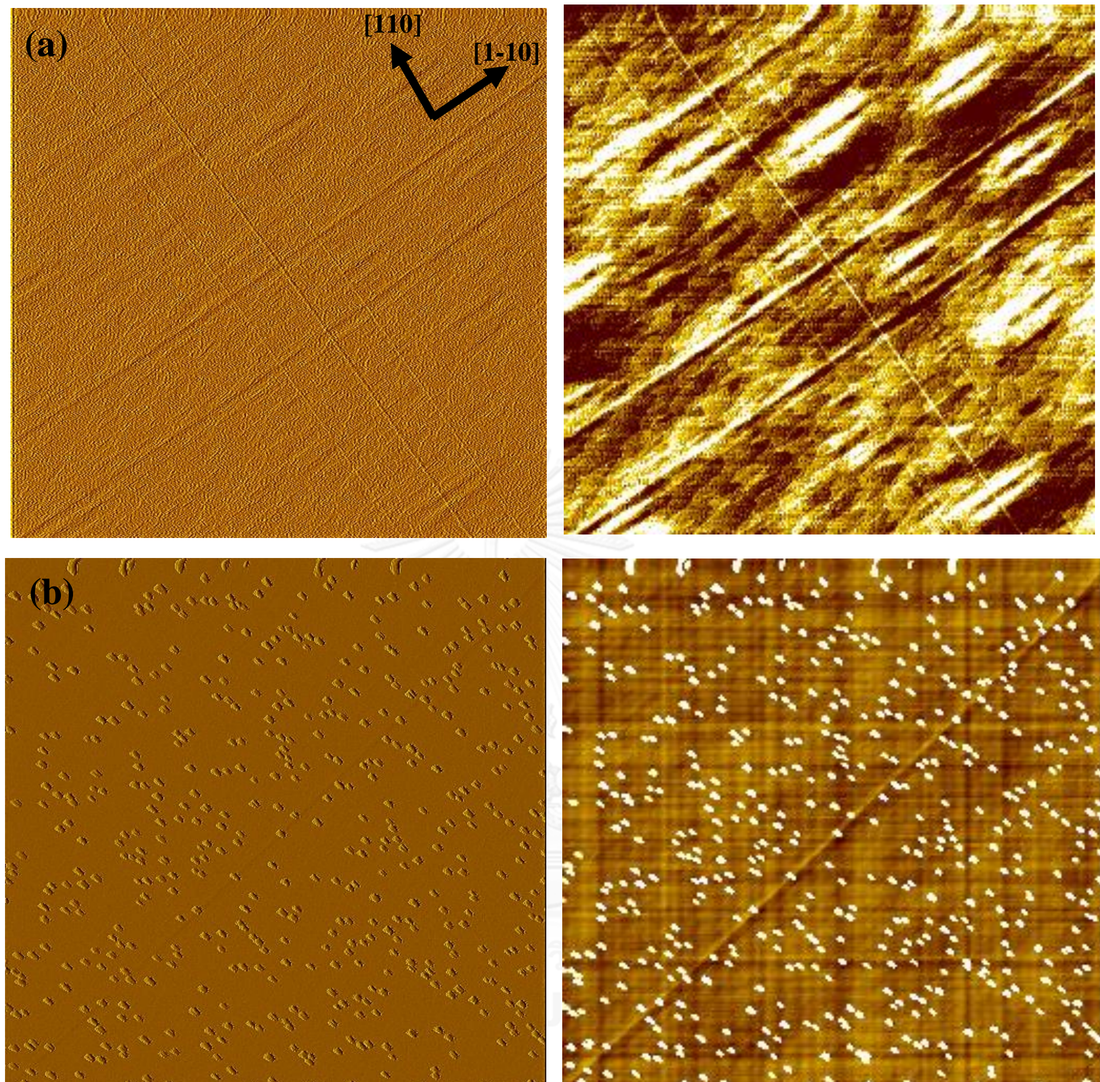

Figure 4.12 5×5 μm^2-AFM images of InSb QDs, grown at (a) 400˚C and (b) 300˚C and their particular height contrast image mode.

The growth of InSb QDs on 30-nm $In_{0.17}Ga_{0.83}As$ CHP at 400˚C results no InSb QDs formation on the surface, as shown in figure 4.12(a). Figure 4.12(b) shows the InSb QDs grown at 300˚C. According to the figure, it seems that CHP does not influence much on the nucleation of InSb QDs to align along the strained sites compare to the InSb QDs nucleation on the rest of flat area. Instead, InSb QDs tend to align and elongate their shape parallel to [110]-direction.

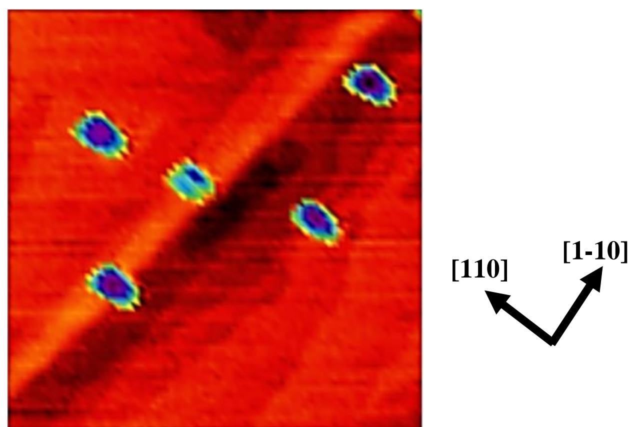

Figure 4.13 Elongated shape of InSb QDs along [110].

As shown in figure 4.13, the shape of InSb QDs are found to elongate parallel to [110]-crystallographic direction which this phenomena is also observed in the InSb/GaAs [4] and InSb/InAs. It is not as same as the QDs shape found in GaSb QDs, even along the CHP ridges, InSb QD seems not to expand its shape out to [1-10]-direction. The average value of their height, width along [1-10] and length along [110] are approximately 8 nm, 70 nm, and 115 nm, respectively.

4.4.2 Morphology: Effect of MEE Technique

As the alignment of GaSb QDs on CHP is successively guided by the compressive strain from CHP, when MEE is performed (see section 4.3). In the same way, MEE technique is also applied to the study the effect of compressive strain in guiding InSb QDs nucleation. To do so, the growth of InSb QDs is done at substrate

temperature of 300˚C and the shutters duty cycle is set to be 20-s Sb, 5s-In, 5s-growth interruption.

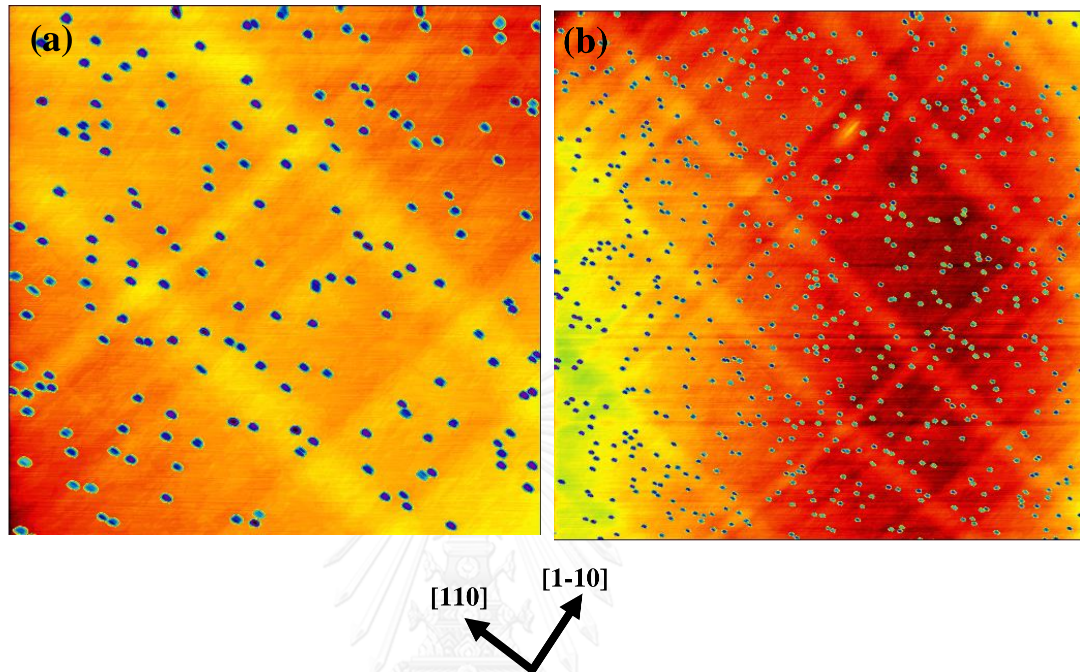

Figure 4.14 (a) 5×5 μm^2 and (b) 10×10 μm^2 modified color AFM image of InSb QDs on CHP template, grown by MEE technique at substrate temperature of 300°C.

จุฬาลงกรณ์มหาวิทยาลัย
CHULALONGKORN UNIVERSITY

Figure 4.14 shows the AFM images in color gradient mode. The morphology shows the re-grown InSb QDs on CHP over the 100-nm capping layer. According to the images, deformed CHP pattern occurred during the capping process. This deformation widens the strain energy distribution along the ridge width. However, based on island nucleation theory, more number of InSb QDs should be found to nucleate along the deformed CHP where the strain energy is relieved. Based on the results, the preferential sites for InSb QDs formation is the flat areas. Two assumptions can be given as follows. (1) The atomic size of InSb is bigger than that of GaSb, which obstruct the atoms to overcome the maximum strain at the edges of CHP ridges. (2) The high lattice-mismatched (~14%) between InSb and CHP leads the

InSb forming on less strained area just to decrease the stress in the system as much as possible.

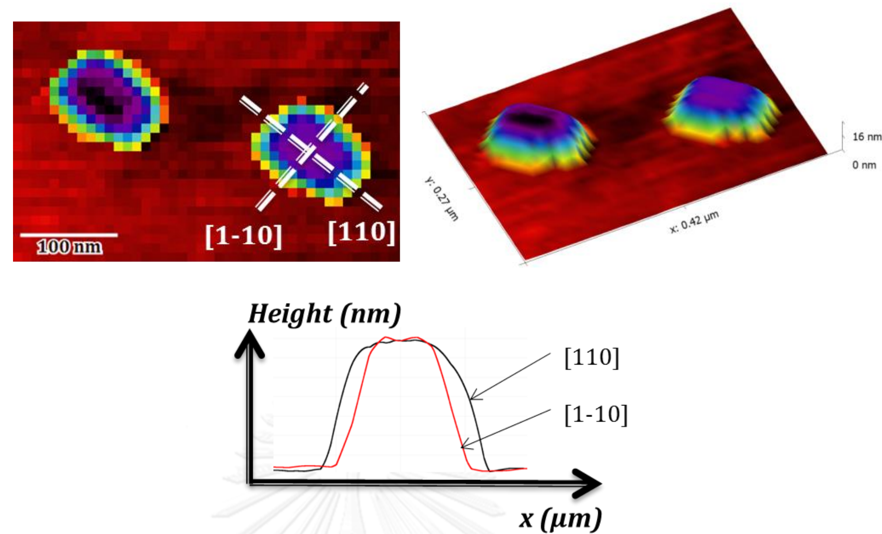

Figure 4.15 The shape configurations of InSb QDs found on the CHP template and the line profiles.

According to figure 4.15, their shapes are elongated to [110], this configuration is similar to the case of InSb QDs grown on GaAs[4]. The line profile of QDs shows a strong asymmetric configuration with the rectangular based shape. The mean value of height, width along [1-10], and length along [110] shows that the mean values of QDs grown by MEE technique are greater than that of QDs grown by conventional method which is approximately 14 nm, 105 nm, and 135 nm, respectively.

Another experimental proof based on the nucleation of InSb QDs along the anti-phase domain (APD) boundary found in GaAs/Ge material system have been conducted. Even the growth is performed at 450°C, the InSb QDs are still observed only along the APD with circular in shape.

CHAPTER 5
CONCLUSIONS

This thesis reports the studies of guiding effect of strain in CHP to the antimonide QDs nucleation. All samples were grown by MBE and different growth techniques, conventional and MEE, are performed. Ex situ characterization was carried out by AFM and PL.

The thickness of InGaAs with the indium content of 17% was optimize to obtain narrow width and low density ridges. The 30-nm $In_{0.17}Ga_{0.83}As$ was set as a template for antimonide QDs growth.

Surface morphology showed the nucleation sites of GaSb QDs, grown by conventional technique, were on both CHP and flat area, whereas GaSb QDs grown by MEE preferred to nucleate along the CHP ridges and even on oval defects caused by substrate overheating. In particular, Sb reduction in MEE enhanced Ga atoms to migrate further and nucleated at the lowest strain energy area. The average height of GaSb QDs on the CHP ridges, grown by MEE, was almost two times higher than that of QDs grown by conventional technique. Moreover, some GaSb QDs were elongated and fit their shape within/along the CHP ridges.

จุฬาลงกรณ์มหาวิทยาลัย
CHULALONGKORN UNIVERSITY

Power-dependent PL of capped GaSb QDs grown by MEE was measured. Side-emission PL showed the energy peaks at ~0.73-0.75 eV and ~1.14 eV, which match and are corresponding to the carrier recombination between GaSb QDs and InGaAs and GaAs, respectively. Even though, these structures are type-II structures, no energy shift was observed. This might be due to limitation of optical equipment for mid- and far-IR detection in our set-up.

The strain in CHP did not influence much to the InSb QD nucleation. Instead, the preferential sites for InSb QDs were the flat areas where the tensile strain (GaAs/InGaAs) dominated.

This thesis experiments are done to understand the guiding effect of strain to the antimonide QDs nucleation. The self-assembled antimonide QDs on self-relieved CHP strain is successfully demonstrated for the first time since many theoretical studies has been proven. The results pave the way for further study on self-aligned antimonide QDs on CHP. In addition, growth temperature and Ga deposition time in MEE are the key parameters that the author would suggest to be optimized in obtaining well-aligned QDs and polarization property, which are the criteria requirements for some applications, i.e. lasers, memory devices, and single electron transistors.

REFERENCES

[1] B. R. Bennett, R. Magno, J. B. Boos, W. Kruppa, and M. G. Ancona, "Antimonide-based compound semiconductors for electronic devices: A review," *Solid-State Electronics,* vol. 49, pp. 1875-1895, 2005.

[2] J. G. Champlain, R. Magno, D. Park, H. S. Newman, and J. Brad Boos, "High-frequency, 6.2ÅpN heterojunction diodes," *Solid-State Electronics,* vol. 67, pp. 105-108, 2012.

[3] B. R. Bennett, P. M. Thibado, M. E. Twigg, E. R. Glaser, R. Magno, B. V. Shanabrook*, et al.*, "Self-assembled InSb and GaSb quantum dots on GaAs(001)," *Journal of Vacuum Science & Technology B,* vol. 14, pp. 2195-2198, 1996.

[4] T. Poempool, n. Zon, S. Kiravittaya, S. Sopitpan, S. Thainoi, S. Kanjanachuchai*, et al.*, "GaSb and InSb Quantum Nanostructures: Morphologies and Optical Properties," *MRS Advances,* vol. FirstView, pp. 1-6, 2015.

[5] D. K. Ferry, Stephen M. Goodnick, and J. Bird., *Transport in Nanostructures*: Cambridge University Press, 2009.

[6] V. P. Kunets, M. Rebello Sousa Dias, T. Rembert, M. E. Ware, Y. I. Mazur, V. Lopez-Richard*, et al.*, "Electron transport in quantum dot chains: Dimensionality effects and hopping conductance," *Journal of Applied Physics,* vol. 113, p. 183709, 2013.

[7] C. K. Hahn, Y. J. Park, E. K. Kim, S.-K. Min, S. K. Jung, and J. H. Park, "Selective formation of one- and two-dimensional arrayed InGaAs quantum dots using Ga2O3 thin film as a mask material," *Applied Physics Letters,* vol. 73, pp. 2479-2481, 1998.

[8] Z. M. Wang, K. Holmes, Y. I. Mazur, and G. J. Salamo, "Fabrication of (In,Ga)As quantum-dot chains on GaAs(100)," *Applied Physics Letters,* vol. 84, pp. 1931-1933, 2004.

[9] C. C. Thet, S. Panyakeow, and S. Kanjanachuchai, "Growth of InAs quantum-dot hatches on InGaAs/GaAs cross-hatch virtual substrates," *Microelectronic Engineering,* vol. 84, pp. 1562-1565, 5// 2007.

[10] V. Gottschalch, "Pallab Bhattacharya (ed.). Properties of lattice-matched and strained indium gallium arsenide. Electronic Materials Information Service, EMIS Datareviews Series No. 8 (Series Advisor: Dr. B. L. Weiss). INSPEC, the Institution of Electrical Engineers, Michael Farday House, Six Hills Way, Stevenage, Herts SG1 2AY, United Kingtom, 1993, 317 Seiten, zahlreiche Abbildungen und Tabellen, Quellennachweise, Sachwörterverzeichnis, ISBN 0-85296-865-5, Preis: 115 £," *Crystal Research and Technology,* vol. 29, pp. 702-702, 1994.

[11] K. Chang, R. Gibala, D. Srolovitz, P. Bhattacharya, and J. Mansfield, "Crosshatched Surface-Morphology In Strained Iii-V Semiconductor-Films," *Journal Of Applied Physics,* vol. 67, p. 4093, 1990.

[12] W. Li, S. Varlamov, M. Jung, and J. Huang, "Vapour-Phase and Solid-Phase Epitaxy of Silicon on Solid-Phase Crystallised Seed Layers for Solar Cells Application," *International Journal of Photoenergy,* vol. 2014, p. 9, 2014.

[13] E. Kuphal, "Liquid phase epitaxy," *Applied Physics A,* vol. 52, pp. 380-409.
[14] K. Ploog, "Molecular Beam Epitaxy of III-V Compounds: Technology and Growth Process," *Annual Review of Materials Science,* vol. 11, pp. 171-210, 1981.
[15] J. Heffernan, M. Kauer, S. E. Hooper, V. Bousquet, and K. Johnson, "InGaN violet laser diodes grown by Molecular Beam Epitaxy," *physica status solidi (a),* vol. 201, pp. 2668-2671, 2004.
[16] R. C. Jaeger, *Introduction to microelectronic fabrication*: Addison-Wesley Longman Publishing Co., Inc., 1987.
[17] J. S. Blakemore, "Semiconducting and other major properties of gallium arsenide," *Journal of Applied Physics,* vol. 53, pp. R123-R181, 1982.
[18] P. S. Dutta, H. L. Bhat, and V. Kumar, "The physics and technology of gallium antimonide: An emerging optoelectronic material," *Journal of Applied Physics,* vol. 81, pp. 5821-5870, 1997.
[19] K. F. Hulme and J. B. Mullin, "Indium antimonide—A review of its preparation, properties and device applications," *Solid-State Electronics,* vol. 5, pp. 211-IN10, 1962/07/01 1962.
[20] K. L. Kavanagh, M. A. Capano, L. W. Hobbs, J. C. Barbour, P. M. J. Marée, W. Schaff*, et al.*, "Asymmetries in dislocation densities, surface morphology, and strain of GaInAs/GaAs single heterolayers," *Journal of Applied Physics,* vol. 64, pp. 4843-4852, 1988.
[21] M. Tamura, A. Hashimoto, and Y. Nakatsugawa, "Threading dislocations in InxGa1−xAs/GaAs heterostructures," *Journal of Applied Physics,* vol. 72, pp. 3398-3405, 1992.
[22] A. M. Andrews, R. LeSar, M. A. Kerner, J. S. Speck, A. E. Romanov, A. L. Kolesnikova*, et al.*, "Modeling crosshatch surface morphology in growing mismatched layers. Part II: Periodic boundary conditions and dislocation groups," *Journal of Applied Physics,* vol. 95, pp. 6032-6047, 2004.
[23] A. E. Romanov, W. Pompe, S. Mathis, G. E. Beltz, and J. S. Speck, "Threading dislocation reduction in strained layers," *Journal of Applied Physics,* vol. 85, pp. 182-192, 1999.
[24] A. M. Andrews, J. S. Speck, A. E. Romanov, M. Bobeth, and W. Pompe, "Modeling cross-hatch surface morphology in growing mismatched layers," *Journal of Applied Physics,* vol. 91, pp. 1933-1943, 2002.
[25] P. Bhattacharya, "Properties of Lattice-Matched and Strained Indium Gallium Arsenide," ed: Institution of Engineering and Technology.
[26] M. Sugawara, *Self-assembled InGaAs/GaAs quantum dots*. San Diego, CA: Academic Press, 1999.
[27] T. Nishioka, Y. Itoh, A. Yamamoto, and M. Yamaguchi, "Crosshatch patterns in GaAs films on Si substrates due to thermal strain in annealing processes," *Applied Physics Letters,* vol. 51, pp. 1928-1930, 1987.
[28] I. Koichi, A. Masahiro, and N. Seiji, "Misfit and Threading Dislocations in GaAs Layers Grown on Si Substrates by MOCVD," *Japanese Journal of Applied Physics,* vol. 26, p. L163, 1987.
[29] M. Albrecht, S. Christiansen, J. Michler, W. Dorsch, H. P. Strunk, P. O. Hansson*, et al.*, "Surface ripples, crosshatch pattern, and dislocation

formation: Cooperating mechanisms in lattice mismatch relaxation," *Applied Physics Letters,* vol. 67, pp. 1232-1234, 1995.

[30] E. A. Fitzgerald, M. T. Currie, S. B. Samavedam, T. A. Langdo, G. Taraschi, V. Yang*, et al.*, "Dislocations in Relaxed SiGe/Si Heterostructures," *physica status solidi (a),* vol. 171, pp. 227-238, 1999.

[31] C. C. Thet, S. Sanorpim, S. Panyakeow, and S. Kanjanachuchai, "The effects of relaxed InGaAs virtual substrates on the formation of self-assembled InAs quantum dots," *Semiconductor Science and Technology,* vol. 23, p. 055007, 2008.

[32] S. Kanjanachuchai, M. Maitreeboriraks, C. C. Thet, T. Limwongse, and S. Panyakeow, "Self-assembled InAs quantum dots on cross-hatch InGaAs templates: Excess growth, growth rate, capping and preferential alignment," *Microelectronic Engineering,* vol. 86, pp. 844-849, 4// 2009.

[33] O. Yastrubchak, T. Wosinski, T. Figielski, E. Lusakowska, B. Pecz, and A. L. Toth, "Misfit dislocations and surface morphology of lattice-mismatched GaAs/InGaAs heterostructures," *Physica E: Low-dimensional Systems and Nanostructures,* vol. 17, pp. 561-563, 4// 2003.

[34] J. W. Matthews and A. E. Blakeslee, "Defects in epitaxial multilayers," *Journal of Crystal Growth,* vol. 27, pp. 118-125, 1974/12/01 1974.

[35] A. Braun, K. M. Briggs, and P. Böni, "Analytical solution to Matthews' and Blakeslee's critical dislocation formation thickness of epitaxially grown thin films," *Journal of Crystal Growth,* vol. 241, pp. 231-234, 5// 2002.

[36] T. G. Andersson, Z. G. Chen, V. D. Kulakovskii, A. Uddin, and J. T. Vallin, "Variation of the critical layer thickness with In content in strained InxGa1−xAs-GaAs quantum wells grown by molecular beam epitaxy," *Applied Physics Letters,* vol. 51, pp. 752-754, 1987.

[37] X. W. Liu, A. A. Hopgood, B. F. Usher, H. Wang, and N. S. J. Braithwaite, "Formation of misfit dislocations during growth of In x Ga 1- x As/GaAs strained-layer heterostructures," *Semiconductor Science and Technology,* vol. 14, p. 1154, 1999.

[38] I. Daruka and A.-L. Barabási, "Dislocation-free island formation in heteroepitaxial growth: a study at equilibrium," *Physical Review Letters,* vol. 79, p. 3708, 1997.

[39] K. Barnham and e. Dimitri Vvedensky, *Low-Dimensional Semiconductor Structures*: Cambridge University Press, 2001.

[40] M. Sugawara. (1999). *Self-assembled InGaAs/GaAS quantum dots*.

[41] M. Asada, Y. Miyamoto, and Y. Suematsu, "Gain and the threshold of three-dimensional quantum-box lasers," *IEEE Journal of Quantum Electronics,* vol. 22, pp. 1915-1921, 1986.

[42] "Front Matter A2 - Henini, Mohamed," in *Molecular Beam Epitaxy*, ed Oxford: Elsevier, 2013, p. iii.

[43] E. H. C. Parker, *The Technology and Physics of Molecular Beam Epitaxy*: Plenum Press, 1985.

[44] M. A. Herman and H. Sitter, *Molecular Beam Epitaxy: Fundamentals and Current Status*: Springer Berlin Heidelberg, 2012.

[45] C. Kittel, *Introduction to Solid State Physics*: Wiley, 2004.

[46] L. M. Peng, S. L. Dudarev, and M. J. Whelan, *High Energy Electron Diffraction and Microscopy*: Oxford University Press, 2004.

[47] A. Y. Cho, "Growth of III–V semiconductors by molecular beam epitaxy and their properties," *Thin Solid Films,* vol. 100, pp. 291-317, 1983/02/25 1983.

[48] H. Yoshiji, K. Minoru, and Y. Hiroshi, "Low-Temperature Growth of GaAs and AlAs-GaAs Quantum-Well Layers by Modified Molecular Beam Epitaxy," *Japanese Journal of Applied Physics,* vol. 25, p. L868, 1986.

[49] Y. Horikoshi, "Surface processes in migration-enhanced epitaxy of III–V compound semiconductors," *Applied Surface Science,* vol. 65, pp. 560-568, 1993/03/02 1993.

[50] K. Kobayashi and E. Ishikawa, "Surface-state conduction through dangling-bond states," *Surface Science,* vol. 540, pp. 431-440, 8/20/ 2003.

[51] A.-L. Barabási, "Self-assembled island formation in heteroepitaxial growth," *Applied Physics Letters,* vol. 70, pp. 2565-2567, 1997.

[52] E. Penev, P. Kratzer, and M. Scheffler, "Effect of strain on surface diffusion in semiconductor heteroepitaxy," *Physical Review B,* vol. 64, p. 085401, 08/01/ 2001.

[53] I. Yonenaga and K. Sumino, "Behaviour of dislocations in GaAs revealed by etch pit technique and X-ray topography," *Journal of Crystal Growth,* vol. 126, pp. 19-29, 1993/01/01 1993.

[54] "Preface A2 - Henini, Mohamed," in *Handbook of Self Assembled Semiconductor Nanostructures for Novel Devices in Photonics and Electronics*, ed Amsterdam: Elsevier, 2008, p. xix.

[55] D. Nečas and P. Klapetek, "Gwyddion: an open-source software for SPM data analysis," *Central European Journal of Physics,* vol. 10, pp. 181-188, 2011.

[56] M. Yano, H. Yokose, Y. Iwai, and M. Inoue, "Surface reaction of III–V compound semiconductors irradiated by As and Sb molecular beams," *Journal of Crystal Growth,* vol. 111, pp. 609-613, 1991/05/02 1991.

[57] K. Akimoto, M. Dohsen, M. Arai, and N. Watanabe, "Origin of oval defects in GaAs layers grown by molecular beam epitaxy," *Journal of Crystal Growth,* vol. 73, pp. 117-122, 1985/10/01 1985.

[58] S. Grosse, J. H. H. Sandmann, G. von Plessen, J. Feldmann, H. Lipsanen, M. Sopanen*, et al.*, "Carrier relaxation dynamics in quantum dots: Scattering mechanisms and state-filling effects," *Physical Review B,* vol. 55, pp. 4473-4476, 02/15/ 1997.

[59] Z. Shuhui, W. Lu, S. Zhenwu, C. Yanxiang, T. Haitao, G. Huaiju*, et al.*, "The structural and optical properties of GaSb/InGaAs type-II quantum dots grown on InP (100) substrate," *Nanoscale Research Letters,* vol. 7, pp. 87-87, 01/25
09/19/received
01/25/accepted 2012.

APPENDIX

จุฬาลงกรณ์มหาวิทยาลัย
Chulalongkorn University

List of Publications

[1] **T. Poempool**, n. Zon, S. Kiravittaya, S. Sopitpan, S. Thainoi, S. Kanjanachuchai, S. Ratanathamaphan, S. Panyakeow, "GaSb and InSb Quantum Nanostructures: Morphologies and Optical Properties," MRS Advances, vol. FirstView: 1-6 (2015).

[2] n. Zon, **T. Poempool**, S. Kiravittaya, S. Sopitpan, S. Thainoi, S. Kanjanachuchai , S. Ratanathamaphan, S. Panyakeow, "Investigation of GaSb/GaAs Quantum Dots Formation on Ge (001) Substrate and Effect of Anti-Phase Domains." MRS Advances FirstView: 1-6 (2016).

[3] **T. Poempool**, Zon, S. Kiravittaya, S. Sopitpan, S. Thainoi, S. Kanjanachuchai, S. Ratanathammaphan, and S. Panyakeow, "InSb/InAs Quantum Nano-Stripes by Molecular Beam Epitaxy," Journal of Vacuum Science & Technology B. (under review)

จุฬาลงกรณ์มหาวิทยาลัย
Chulalongkorn University

VITA

Thanavorn Poempool was born in Phatthalung province, Thailand on February 1, 1992. His currently hometown is Phuket where he was raised and completed the curriculum education. He received the Bachelor of Science in Physics from Chulalongkorn University, Thailand in May 2014.

He continued his education at Semiconductor Device Research Laboratory (SDRL), Department of Electrical Engineering, Chulalongkorn University as a Master Degree student in August 2014. His research interests cover Solid-State Physics, Electromagnetic Theory and Optics: Integrated Photonics, Lab-On-Chip, Silicon Photonics, Nanostructure of Semiconductor, and Molecular Beam Epitaxy.

จุฬาลงกรณ์มหาวิทยาลัย
Chulalongkorn University